Alzheimer's disease risk gene BIN1 modulates neural network activity through the regulation of L-type calcium channel expression in human induced neurons

Orthis Saha[1,#], Ana Raquel Melo de Farias[1,2,#], Alexandre Pelletier[3,#], Dolores Siedlecki-Wullich[1], Johanna Gadaut[1], Bruna Soares Landeira[1], Arnaud Carrier[3], Anaïs-Camille Vreulx[1], Karine Guyot[1], Amelie Bonnefond[3], Philippe Amouyel[1], Cláudio Marcos Queiroz[2], Devrim Kilinc[1], Fabien Delahaye[3], Jean-Charles Lambert[1] and Marcos R. Costa[1,2,*]

1. Univ. Lille, Inserm, CHU Lille, Institut Pasteur de Lille, U1167-RID-AGE facteurs de risque et déterminants moléculaires des maladies liées au vieillissement, DISTALZ, Lille, France
2. Brain Institute, Federal University of Rio Grande do Norte, Natal, Brazil
3. Univ. Lille, Inserm, CNRS, CHU Lille, Institut Pasteur de Lille, U1283-UMR 8199 EGID, Lille, France

# Equal contribution

* Correspondence should be addressed to:

Marcos Costa, MD, PhD
INSERM UMR1167
Institut Pasteur de Lille
1 rue du Pr. Calmette
59019 Lille CEDEX, France
Tel: 00 33 (0)3 20 87 77 10
marcos.costa@pasteur-lille.fr

Abstract

Bridging Integrator 1 (*BIN1*) is the second most important Alzheimer's disease (AD) risk gene after *APOE*, but its physiological roles and contribution to brain pathology are largely elusive. In this work, we tackled the short- and long-term effects of BIN1 deletion in human induced neurons (hiNs) grown in bi-dimensional cultures and in cerebral organoids. We show that *BIN1* loss-of-function leads to specific transcriptional alterations in glutamatergic neurons involving mainly genes associated with calcium homeostasis, ion transport and synapse function. We also show that BIN1 regulates calcium transients and neuronal electrical activity through interaction with the L-type voltage-gated calcium channel $Cav_{1.2}$ and regulation of activity-dependent internalization of this channel. Treatment with the $Cav_{1.2}$ antagonist nifedipine partly rescues neuronal electrical alterations in *BIN1* knockout hiNs. Together, our results indicate that BIN1 misexpression impairs calcium homeostasis in glutamatergic neurons, potentially contributing to the transcriptional changes and neural network dysfunctions observed in AD.

Introduction

The Bridging Integrator 1 (*BIN1*) is the second most associated genetic determinant with the risk of late-onset Alzheimer's disease (LOAD), after the Apolipoprotein E (*APOE*) gene[1–4], and it is only since the report of its association with AD more than ten years ago that its role in brain functions started to be investigated. In the adult human brain, *BIN1* is mainly expressed by oligodendrocytes, microglial cells, glutamatergic and GABAergic neurons[5–7] and its expression is reduced in the brains of AD patients compared to healthy individuals[7–9]. How this reduced expression of *BIN1* may affect AD pathogenesis remains poorly understood.

Changes in *BIN1* expression have been controversially associated with amyloid precursor protein (APP) processing towards the production of amyloid-beta (Aβ) peptides in cellular models[10,11]. However, we recently showed that BIN1 regulates endocytic trafficking in hiPSC-derived neurons (hiNs), without significantly affecting amyloidogenic APP processing[12] and BIN1 underexpression does not modify amyloid pathology in an AD-like mouse model[13]. A direct interaction between TAU and BIN1 has also been reported[14,15] potentially impacting learning and memory in a Tauopathy mouse model[16], Tau phosphorylation and propagation in vitro[16–19] or network hyperexcitability in rat hippocampal neurons[19].

Despite these advances, no consensus has been reached on the role of BIN1 in AD pathogenesis and even its physiological functions in human brain cells remain mostly unknown. Therefore, rather than developing an Ab/Tau-based hypothesis as in most previous reports, we decided to first develop an agnostic approach to capture a BIN1-dependent molecular landscape in cerebral organoids and neural cells derived from hiPSC underexpressing this gene.

Results

Transcriptional alterations in *BIN1* KO hiNs highlight pathways related to electrical activity and synaptic transmission

To unbiasedly study possible changes in gene expression in human neural cells in function of BIN1 expression, we generated *BIN1* wild-type (WT), and knockout (KO) cerebral organoids (COs)[20,21]. After 6.5 months of culture, COs were composed of all the major neural cell types identified by the expression of MAP2, GFAP and NESTIN, and we did not observe any gross differences in size or morphology of COs between genotypes (Fig. 1A). Western blot analyses confirmed the absence of BIN1 protein in *BIN1* KO COs (Fig. 1B). Using snRNA-seq, we recovered the transcriptional profile of 4398 nuclei that were grouped into 7 major cell clusters based on the expression of cell type markers (Fig. 1C-D). As observed in the human brain[7], BIN1 expression in COs was mainly detected in oligodendrocytes and glutamatergic neurons (Fig. 1D). Notably, we observed a significant reduction in the proportion of glutamatergic neurons in *BIN1* KO compared to WT COs (Fig. 1E), suggesting their selective loss or reduced differentiation. Using Wilcoxon test after sctransform normalization and variance stabilization of molecular count data[22], we detected 124, 75, 4 and 1 differently expressed genes (DEGs; |log2FC| >0.25 and FDR <0.05) respectively in glutamatergic neurons, astrocytes, NPCs and oligodendrocytes, when comparing gene expression in single cell populations of *BIN1* KO and WT COs (Fig. 1F; Sup. Table 1). Gene ontology (GO) term enrichment analysis for DEGs identified in *BIN1* KO glutamatergic neurons revealed a significant enrichment for several terms associated with synaptic transmission, calcium binding and ion channels (Fig. 1G; Sup. Table 2). In *BIN1* KO astrocytes, we found enrichment for GO terms associated with neuronal differentiation (Sup. Table 2). In addition, since BIN1 is expressed at very low level in WT COs astrocytes and we noticed several DEGs regulated by neuronal activity, such as *APBA1*, *GRIN2B*, *NPAS3* and *RORA* (Sup. Table 1)[23], changes in astrocytes are likely secondary to neuronal modifications/dysfunctions. Accordingly, we observed 65 DEGs in glutamatergic neurons of *BIN1* heterozygous (HET) compared to WT COs but only 6 DEGs in astrocytes (Sup. Fig. 1). Similar transcriptional alterations were observed in *BIN1* KO hiNs generated in bi-dimensional cultures (Sup. Fig. 2).

We next aimed at evaluating the cell-autonomous effect of *BIN1* deletion in glutamatergic neurons and, for this purpose, we generated *BIN1* WT or KO pure glutamatergic neuronal cultures by direct lineage-reprogramming of human NPCs (hNPCs) using doxycycline-inducible expression of ASCL1 (see online methods). After validation that ASCL1 expression efficiently reprogrammed hNPCs into highly pure neurons (hereafter ASCL1-hiNs; Fig. 1H), we added exogenous human cerebral cortex astrocytes to support functional neuronal maturation and synaptic connectivity[24]. After 4 weeks of differentiation and snRNA-seq analyses (n=3114 from 2 independent culture batches), we observed that ASCL1-hiNs (~70% of all the cells; see Online Methods for a full description of the cellular populations) were composed of glutamatergic neurons (~92%) with a small proportion of GABAergic neurons (~2%) or of cells co-expressing low levels of markers of both neuronal subtypes (~6%). We detected 675 DEGs (|log2FC| >0.25 and FDR <0.05) in *BIN1* KO compared to WT glutamatergic neurons, and only 1 DEG in GABAergic neurons (Fig. 1K; Sup. Table 3). As observed in COs (Fig. 1G) and spontaneously differentiated hiNs (Sup. Fig. 2), GO term enrichment analysis revealed a significant enrichment for terms associated with synaptic transmission, ion channel activity and calcium signaling pathways (Fig. 1L; Sup. Table 4). Noteworthy, exogenously added human astrocytes co-cultured with *BIN1* WT and KO hiNs showed a low number of DEGs (25 in Astro-I and 18 in Astro-II; Sup. Table 3), likely again reflecting an astrocyte reaction to primary changes in hiNs in response to *BIN1* deletion.

Altogether, results obtained from 2D and 3D models indicate that BIN1 loss-of-function leads to specific transcriptional changes associated with functional properties of glutamatergic neurons.

Molecular alterations in *BIN1* KO organoids and hiNs resemble those observed in the brains of AD patients

We then sought to evaluate whether molecular alterations in our neural models may recapitulate some of those observed in the brain of AD cases. For this purpose, we used a publicly available snRNA-seq dataset generated from the entorhinal cortex (EC) and superior frontal gyrus (SFG) of AD patients at different Braak stages[9]. We first observed a progressive and significant decrease in *BIN1* mRNA levels in glutamatergic neurons (Fig. 2A), suggesting that reduced BIN1 expression in this cell type may be a common feature occurring in the AD

pathology progression. We then compared DEGs identified in *BIN1* KO glutamatergic neurons (either from COs or ASCL1-hiNs) with those identified in the same cell subtype of AD brains (Sup. Table 5). Remarkably, DEGs identified in *BIN1* KO glutamatergic neurons (either from COs or ASCL1-hiNs) showed a statistically significant overlap with DEGs detected in this cell population in AD brains at different Braak stages (Fig. 2B). In astrocytes, however, a similar significant overlap could only be observed between COs and AD brains (Fig. 2B). GO analysis based on DEG overlap between *BIN1* KO ASCL1-hiNs and AD brain glutamatergic neurons indicated significant enrichment for pathways associated with glutamate receptor activity and gated channel activity (Fig. 2C). Similarly, DEG overlap between *BIN1* KO COs and AD brain glutamatergic neurons was significantly enriched for genes associated with glutamate receptor activity, gated channel activity and calcium ion binding (Fig. 2D; Sup. Table 6). No significant enrichment was observed for DEG overlap between *BIN1* KO COs and AD brain astrocytes (data not shown). Altogether, these observations suggest that *BIN1* loss-of-function is sufficient to elicit gene expression alterations in glutamatergic neurons in part similar of those observed in AD brains and associated with functional properties of glutamatergic neurons.

We finally investigated if AD-like biochemical modifications may occur in our different models by measuring the levels of phosphorylated TAU, APP, APP CTF-β and Aβ peptides. We detected an increase in the intracellular levels of phospho-TAU (Ser202, Thr205) in *BIN1* KO compared to WT cultures both in 2D and 3D cultures (Fig. 2E-H). In agreement with our previous observations in cerebral organoids (Lambert et al., 2022), we did not detect any significant differences neither in the concentrations of soluble Aβ(1-x) or Aβ(1-42), nor in the intracellular levels of full-length APP and APP CTF-β in *BIN1* KO compared to WT hiN cultures in 2D (Sup. Fig. 3). Altogether, these results indicate that BIN1 underexpression may be sufficient to induce AD-related Tau hyperphosphorylation in glutamatergic neurons.

Number of synaptic contacts is decreased in BIN KO organoids

Since synapse loss is also an early marker of AD development, we then assessed whether BIN1 deletion may affect synaptic connectivity in our different models. Using immunohistochemistry experiments, we did not find any significant differences in the number of putative synaptic contacts (% SYP assigned) in *BIN1* KO compared to WT ASCL1-hiNs, both at 4 and 6 weeks of differentiation (Fig. 3A-D). We also studied glutamatergic

163 synapses functionally using real-time imaging of ASCL1-hiNs expressing glutamate sensor
164 iGLUSnFr[25]. Like our observations based on immunocytochemistry, we did not detect
165 differences neither in the number of glutamatergic synapses (active spots) nor in the
166 frequency of events (change in fluorescence levels in active spots) in *BIN1* KO compared to
167 WT ASCL1-hiNs (Sup. Fig. 4; Sup. Movies 1 and 2). In contrast, *BIN1* KO COs showed a
168 significant reduction in the number of synaptic contacts (Fig. 3H), mainly due to a reduction
169 in the number of post-synaptic spots expressing HOMER1 (Fig. 3E-F). Thus, our data
170 indicate that long term BIN1 underexpression may affect synaptic connectivity, even if not
171 detectable at short term in 2D culture.
172
173 **_BIN1_ null deletion modifies electrical activity pattern in ASCL1-hiNs**
174 Although we cannot exclude that the latter observations may be linked to a difference
175 between 2D and 3D cultures per se, we postulated that the decrease in synaptic contacts
176 after long-term *BIN1* deletion may be a consequence of synapse down-scaling resulting from
177 chronically increased neuronal excitability due to deregulation of functional properties of
178 glutamatergic neurons[41,42]. To directly address this possibility, we used multi-electrode
179 arrays (MEA) to record and quantify multi-unit activity (MUA) in ASCL1-hiNs cultured in a
180 microfluidic device, which guides neurites into microchannels that are positioned over
181 recording electrodes (Sup. Fig. 5). As observed in dissociated cultures of cortical cells[26], 2D
182 cultures of ASCL1-hiNs cells exhibited a diverse range of spontaneous activity patterns,
183 including regular discharges, population bursts and period activity (Sup. Fig. 4). In this
184 respect, we found a conspicuous change in the temporal organization of MUA after *BIN1*
185 deletion, mainly characterized by an increased number of spike bursts at 4 weeks (Sup. Fig.
186 4). These alterations may result from compensatory adjustments in neuronal connectivity,
187 intrinsic membrane properties or both. To disentangle these possibilities, we used
188 waveform-based spike sorting to examine the functional consequences of *BIN1* deletion at
189 the single neuronal level (Fig. 4). We identified a similar number of single units per recording
190 electrode between genotypes (WT: 4.92±2.34; KO: 5.27±2.45), indicating that *BIN1* deletion
191 does not impair the expression neither the density of active units within culture
192 microchannels. However, we observed reduced single-unit activity (SUA) frequency (Fig. 4B)
193 and increased SUA amplitude (Fig. 4C) in *BIN1* KO compared to WT ASCL1-hiNs.
194 Interestingly, we could not detect significant changes in the number of bursts per neuron

(WT: 11.01±6.71; KO: 10.36±8.59), although the burst duration and the number of spikes within a burst were significantly decreased in *BIN1* KO compared to WT ASCL1-hiNs (Fig. 4D-E), demonstrating the pertinence of performing spike sorting in MEA data. With this approach, we demonstrate the temporal disorganization observed in *BIN1* KO hiNs networks (Fig. 4F) by computing the array-wide spike detection rate (ASDR), which reveals the strength of the synchronized population activity, and the autocorrelograms of SUAs, which allows the apprehension of synchronized periodicity. Both methods revealed striking modifications in the temporal organization of SUAs in *BIN1* KO compared to WT ASCL1-hiNs (Fig. 4G-I). While most spikes of *BIN1* WT neurons occurred at periodic intervals of about 8-10 s, the spikes of *BIN1* KO neurons were randomly distributed, suggesting that *BIN1* deletion in neurons impairs the capacity of these cells to generate organized patterns of electrical activity. Accordingly, the percentage of spikes occurring outside of bursts was significantly higher in *BIN1* KO than in WT ASCL1-hiNs (Fig. 4J).

Acute MEA recordings in 5-month-old COs also revealed a significant increase in spike frequency in *BIN1* KO compared to WT COs (Fig. 5A-B), but these experiments represent a very narrow time shot of COs differentiation. Therefore, to evaluate chronic alterations in neuronal electrical activity in this system, we developed an original approach based on the expression of activity-related genes (ARGs)[27]. While neurons stimulated with brief patterns of electrical activity transcribe rapid primary response genes (rPRGs) or early response genes (ERGs), those stimulated with sustained patterns of electrical activity express delayed primary response genes (dPRGs), secondary response genes (SRGs) and late response genes (LRGs) (Fig. 5C)[28,29]. Using Cell-ID[30], we analyzed the enrichment for these gene signatures (Sup. Table 7) in our COs at single-cell resolution. As expected, we observed that ARG signatures were predominantly enriched in neurons (Fig. 5D). Quantification of the proportion of neurons significantly enriched for specific signatures (p_{adj}<0.05) revealed a significantly higher proportion of glutamatergic neurons enriched for dPRGs, SRGs and LRGs in *BIN1* KO compared to WT COs (Fig. 5E). Enrichments for SRGs and LRGs were specific for this cell type and could not be observed either in GABAergic neurons (Fig. 5E) or in *BIN1* HET glutamatergic neurons (Sup. Fig. 6). Thus, *BIN1* deletion leads to alterations in neuronal electrical activity before observable changes in synaptic connectivity, suggesting that functional changes in *BIN1* KO ASCL1-hiNs are likely a consequence of altered cell-intrinsic properties.

227

228 **BIN1 regulates neuronal Ca^{2+} dynamics through LVGCCs**

229 Since we found significant enrichment for several terms associated with calcium
230 binding and ion channels, we postulated that actors of these pathways may be responsible
231 for such altered cell-intrinsic properties. To probe whether Ca^{2+} dynamics was altered in
232 *BIN1* KO ASCL1-hiNs, we performed calcium imaging in 4-week-old cultures (Sup. Movies 3
233 and 4). We observed a significant increase in the frequency of Ca^{2+} transients in *BIN1* KO
234 compared to WT ASCL1-hiNs, associated with changes in fluorescence dynamics indicative
235 of longer times to reach the maximum intracellular Ca^{2+} levels and to recover baseline levels
236 (Fig. 6A-F).

237 LVGCCs are key regulators of Ca^{2+} transients in neurons, which play a fundamental role
238 in neuronal firing and gene transcription regulation[31]. We thus sought to determine if BIN1
239 may interact and regulate LVGCC expression in hiNs, as previously described for
240 cardiomyocytes[32]. First, we performed proximity ligation assay (PLA) to probe a possible
241 interaction between BIN1 and $Cav1_{.2}$ or $Cav_{1.3}$, the two LVGCCs expressed in ASCL1-hiNs
242 (Sup. Fig. 7). We observed a widespread BIN1-$Cav_{1.2}$ PLA signal (Fig. 6G) and, to a lesser
243 extent, a BIN1-$Cav_{1.3}$ one in neurons (Sup. Fig. 7). Next, we quantified neuronal LVGCC
244 protein level and observed an increase in total $Cav_{1.2}$ levels in *BIN1* KO compared to WT
245 ASCL1-hiNs (Fig. 6H-I). Protein levels of neither $Cav_{1.3}$, nor the members of the Cav_2 family
246 ($Cav_{2.1}$, $Cav_{2.2}$ and $Cav_{2.3}$) were increased in the same cultures (Sup. Fig. 7), suggesting a
247 specific regulation of $Cav_{1.2}$ expression by BIN1.

248 Notably, LVGCCs are key regulators of the synchronous firing pattern in neurons[33] and
249 one of the homeostatic mechanisms protecting neurons from hyperexcitability involves
250 activity-dependent internalization of those channels[34]. Thus, to evaluate whether BIN1
251 deletion may impair this mechanism, we stimulated ASCL-hiNs with KCl 65nM for 30 min
252 and collected total and endosomal proteins for analysis. We confirmed an increase in the
253 global level of $Cav_{1.2}$ in BIN1 KO ASCL1-hiNs that was independent of KCl treatment (Fig. 6J).
254 However, $Cav_{1.2}$ expression in the endosomal fraction was increased by 50% after KCl
255 treatment in BIN1 WT, whereas this increase was only of 10% in BIN1 KO ASCL1-hiNs (Fig.
256 6K). This effect was specific for $Cav_{1.2}$ since both early endosome antigen 1 (EEA1) and $Cav_{1.3}$
257 expression increased in both BIN1 WT and KO ASCL1-hiNs at similar levels after KCl
258 treatment (Fig. 6K).

These last observations prompted us to investigate whether the network dysfunctions observed in *BIN1* KO ASCL1-hiNs may be related to the increased $Cav_{1.2}$ protein levels. For this purpose, we treated these cells with nifedipine, a specific antagonist of $Cav_{1.2}$ at a physiologically relevant concentration (50 nM) for 2 weeks. We observed a partial recovery of the oscillatory pattern of neuronal electrical activity observed in WT cells (Fig. 6L). Interestingly, the percentage of spikes outside bursts was not affected by nifedipine treatment in *BIN1* WT, but significantly decreased in *BIN1* KO ASCL-hiNs (Fig. 6M), indicating a partial recovery of burst organization. To note, no difference in firing rates was observed whatever the models and conditions (Fig. 6N). Altogether, these data support the view that BIN1 contributes to the regulation of electrical activity through the regulation of $Cav_{1.2}$ expression/localization in human neurons.

Discussion

In this work, we show that the AD genetic risk factor *BIN1*, plays a critical role in the regulation of neuronal firing homeostasis in glutamatergic neurons. Complete deletion of *BIN1* gene in these neurons is sufficient to alter the expression of the LVGCC $Cav_{1.2}$, leading to altered calcium homeostasis and neural network dysfunctions in human neurons *in vitro*. These functional changes are correlated with changes in the expression of genes involved in synaptic transmission and ion transport across the membrane, as well as increased Tau phosphorylation. In long-term neuronal cultures using COs, we confirm that *BIN1* loss-of-function affects electrical activity and leads to synapse loss, transcriptional and biochemical alterations resembling those observed in the AD brain. These results suggest that misexpression of BIN1 in glutamatergic neurons may contribute to early stages of AD pathophysiology by dysregulating neuronal firing homeostasis through LVGCCs.

Neuronal network dysfunctions are observed in AD patients at early stages of the disease and precede or coincide with cognitive decline [35–37]. Under physiological conditions, neuronal networks can maintain optimal output through regulation of synaptic and cell-intrinsic mechanisms[38]. Our results suggest that normal levels of BIN1 expression in glutamatergic neurons are fundamental to regulate neuronal firing rate homeostasis. Indeed, *BIN1* deletion in hiNs is sufficient to dysregulate network oscillations even without impacting the number of functional synaptic contacts, suggesting that the desynchronization observed in *BIN1* KO hiNs circuits are a consequence of miscarried homeostatic controls of neuronal activity.

One key mechanism controlling neuronal spiking activity is the regulation of Ca^{2+} homeostasis [31,33,39]. Increased neuronal electrical activity induces the turnover of LVGCCs from the plasma membrane through endocytosis[34] and regulates the transcription of genes encoding for calcium-binding proteins and calcium-mediated signaling[40], mechanisms aiming to restore local Ca^{2+} signaling cascades and protect cells against aberrant Ca^{2+} influx. We show that BIN1 interacts with $Cav_{1.2}$ in hiNs, similar to previous findings in cardiac T tubules[32] and in mouse hippocampal neurons[19] and provide evidence supporting a novel role for BIN1 in the regulation of activity-dependent internalization of $Cav_{1.2}$ in human neurons, thus linking BIN1 to firing homeostasis in human neurons through that LTVGCC.

Loss of Ca^{2+} homeostasis is an important feature of many neurological diseases and has been extensively described in AD[41,42]. Interestingly, DEGs identified in glutamatergic neurons in our different cell culture models are enriched for calcium-related biological processes. This is also observed for DEGs detected both in glutamatergic neurons of *BIN1* KO COs and in AD brains. Thus, reduced expression of *BIN1* in glutamatergic neurons may contribute to the breakdown of Ca^{2+} homeostasis in the AD brain, potentially contributing to neuronal circuit dysfunctions. Consistent with this hypothesis, we have previously shown a significant reduction in the expression of the transcript encoding for the neuron-specific BIN1 isoform 1 in bulk RNA-sequencing data from a large number of AD patients[7] and we show in this work that *BIN1* expression is reduced in glutamatergic neurons of AD brains at late Braak stages.

Altogether, our results suggest that *BIN1* misexpression in glutamatergic neurons may primarily undermine Ca^{2+} homeostasis, leading to changes in neuronal electrical activity. In a later stage, gene expression and circuit-level alterations such as synapse loss would occur, likely because of altered neuronal electrical activity. A corollary to this model would be that early treatments aiming to restore Ca^{2+} homeostasis and neuronal electrical activity may have a beneficial impact in AD. Interestingly, a Mendelian randomization and a retrospective population-based cohort study found evidence suggesting that Ca^{2+} channel blockers are associated with a reduced risk of AD[43,44]. In the future, it would be interesting to study the impact of these drugs for AD onset/progress as a function of genetic variants in the *BIN1* locus.

Acknowledgements and financial support

The authors thank the BICeL platform of the Institut Biologie de Lille and the Vect'UB viral platform (INSERM US 005 – CNRS 3427 – TBMCore, Université de Bordeaux, France). The authors thank Karine Blary at the IEMN Lille for the microfabrication work. The Maestro Pro multiwell microelectrode array was acquired with the "Prix Claude Pompidou pour la Recherche sur l'Alzheimer (2021)" to MRC. This work was co-funded by the European Union under the European Regional Development Fund (ERDF) and by the Hauts de France Regional Council (contract no.18006176), the MEL (contract_2016_ESR_05), and the French State (contract no. 2018-3-CTRL_IPL_Phase2). This work was partly supported by the French RENATECH network (P-18-02737), Fondation pour la recherche médicale (ALZ201912009628, ALZ201906008477), PTR-MIAD, Fondation Recherche Alzheimer and by the Sanofi i-Awards Europe 2019. This work was also funded by the Lille Métropole Communauté Urbaine and the French government's LABEX DISTALZ program (Development of innovative strategies for a transdisciplinary approach to Alzheimer's disease). The UMR 8199 LIGAN-PM Genomics platform (Lille, France) belongs to the 'Federation de Recherche' 3508 Labex EGID (European Genomics Institute for Diabetes; ANR-10-LABX-46) and was supported by the ANR Equipex 2010 session (ANR-10-EQPX-07-01; 'LIGAN-PM'). The LIGAN-PM Genomics platform (Lille, France) is also supported by the FEDER and the Region Nord-Pas-de-Calais-Picardie and is a member of the "France Génomique" consortium (ANR-10-INBS-009).

Declaration of interests

The authors declare no competing interests.

Author contributions

Conceptualization, M.R.C.; Methodology, M.R.C., F.D., D.K., C.M.Q.; Investigation, M.R.C., O.S., B.S.L., A.R.M.F., A.C., A.P., D.S.W., F.D., K.G., D.K., C.M.Q.; Writing - Original Draft, M.R.C.; Writing - Reviews & Editing, M.R.C., F.D., J.C.L., C.M.Q., D.K.; Figures preparation: M.R.C., F.D., A.P., B.S.L., A.R.M.F., D.K. Supervision, M.R.C., F.D., J.C.L., D.K.; Funding Acquisition, M.R.C., J.C.L., F.D, D.K., P.A., A.B. All authors have read and approved the manuscript.

References

1. Lambert, J. C. *et al.* Meta-analysis of 74,046 individuals identifies 11 new susceptibility loci for Alzheimer's disease. *Nat. Genet.* **45**, 1452–1458 (2013).
2. Kunkle, B. W. *et al.* Genetic meta-analysis of diagnosed Alzheimer's disease identifies new risk loci and implicates Aβ, tau, immunity and lipid processing. *Nat. Genet.* **51**, 414–430 (2019).
3. Bellenguez, C., Küçükali, F., Jansen, I., Andrade, V. & Moreno-grau, S. New insights on the genetic etiology of Alzheimer ' s and related dementia. 1–35 (2020).
4. Schwartzentruber, J. *et al.* Genome-wide meta-analysis, fine-mapping and integrative prioritization implicate new Alzheimer's disease risk genes. *Nat. Genet.* **53**, 392–402 (2021).
5. De Rossi, P. *et al.* Predominant expression of Alzheimer's disease-associated BIN1 in mature oligodendrocytes and localization to white matter tracts. *Mol. Neurodegener.* **11**, (2016).
6. De Rossi, P. *et al.* Neuronal BIN1 Regulates Presynaptic Neurotransmitter Release and Memory Consolidation. *Cell Rep.* **30**, 3520-3535.e7 (2020).
7. Marques-Coelho, D. *et al.* Differential transcript usage unravels gene expression alterations in Alzheimer's disease human brains. *npj Aging Mech. Dis.* **7**, 2 (2021).
8. Glennon, E. B. C. *et al.* BIN1 Is Decreased in Sporadic but Not Familial Alzheimer's Disease or in Aging. *PLoS One* **8**, 1–11 (2013).
9. Leng, K. *et al.* Molecular characterization of selectively vulnerable neurons in Alzheimer's disease. *Nat. Neurosci.* **24**, 276–287 (2021).
10. Ubelmann, F. *et al.* Bin1 and CD 2 AP polarise the endocytic generation of beta-amyloid . *EMBO Rep.* **18**, 102–122 (2017).
11. Miyagawa, T. *et al.* BIN1 regulates BACE1 intracellular trafficking and amyloid-β production. *Hum. Mol. Genet.* **25**, 2948–2958 (2016).
12. Lambert, E. *et al.* The Alzheimer susceptibility gene BIN1 induces isoform-dependent neurotoxicity through early endosome defects. *Acta Neuropathol. Commun.* **10**, 4 (2022).
13. Andrew, R. J. *et al.* Reduction of the expression of the late-onset Alzheimer's disease (AD) risk-factor BIN1 does not affect amyloid pathology in an AD mouse model. *J. Biol. Chem.* **294**, 4477–4487 (2019).

14. Chapuis, J. *et al.* Increased expression of BIN1 mediates Alzheimer genetic risk by modulating tau pathology. *Mol. Psychiatry* **18**, 1225–1234 (2013).
15. Sottejeau, Y. *et al.* Tau phosphorylation regulates the interaction between BIN1's SH3 domain and Tau's proline-rich domain. *Acta Neuropathol. Commun.* **3**, 58 (2015).
16. Sartori, M. *et al.* BIN1 recovers tauopathy-induced long-term memory deficits in mice and interacts with Tau through Thr348 phosphorylation. *Acta Neuropathol.* **138**, 631–652 (2019).
17. Calafate, S., Flavin, W., Verstreken, P. & Moechars, D. Loss of Bin1 Promotes the Propagation of Tau Pathology. *Cell Rep.* **17**, 931–940 (2016).
18. Lasorsa, A. *et al.* Structural basis of tau interaction with BIN1 and regulation by tau phosphorylation. *Front. Mol. Neurosci.* **11**, 1–12 (2018).
19. Voskobiynyk, Y. *et al.* Alzheimer's disease risk gene BIN1 induces Tau-dependent network hyperexcitability. *Elife* **9**, 1–25 (2020).
20. Lancaster, M. A. *et al.* Cerebral organoids model human brain development and microcephaly. *Nature* **501**, 373–379 (2013).
21. Trujillo, C. A. *et al.* Complex Oscillatory Waves Emerging from Cortical Organoids Model Early Human Brain Network Development. *Cell Stem Cell* **25**, 558-569.e7 (2019).
22. Hafemeister, C. & Satija, R. Normalization and variance stabilization of single-cell RNA-seq data using regularized negative binomial regression. *bioRxiv* 1–15 (2019) doi:10.1101/576827.
23. Farhy-Tselnicker, I. *et al.* Activity-dependent modulation of synapse-regulating genes in astrocytes. doi:10.7554/eLife.
24. Christopherson, K. S. *et al.* Thrombospondins are astrocyte-secreted proteins that promote CNS synaptogenesis. *Cell* **120**, 421–433 (2005).
25. Marvin, J. S. *et al.* Stability, affinity, and chromatic variants of the glutamate sensor iGluSnFR. *Nat. Methods* **15**, 936–939 (2018).
26. Wagenaar, D. A., Pine, J. & Potter, S. M. An extremely rich repertoire of bursting patterns during the development of cortical cultures. *BMC Neurosci.* **7**, 1–18 (2006).
27. Flavell, S. W. & Greenberg, M. E. Signaling Mechanisms Linking Neuronal Activity to Gene Expression and Plasticity of the Nervous System. *Annu. Rev. Neurosci.* **31**, 563–590 (2008).

28. Tyssowski, K. M. *et al.* Different Neuronal Activity Patterns Induce Different Gene Expression Programs. *Neuron* **98**, 530-546.e11 (2018).
29. Hrvatin, S. *et al.* Single-cell analysis of experience-dependent transcriptomic states in the mouse visual cortex. *Nat. Neurosci.* **21**, 120–129 (2018).
30. Cortal, A., Martignetti, L., Six, E. & Rausell, A. Gene signature extraction and cell identity recognition at the single-cell level with Cell-ID. *Nat. Biotechnol.* (2021) doi:10.1038/s41587-021-00896-6.
31. Simms, B. A. & Zamponi, G. W. Neuronal voltage-gated calcium channels: Structure, function, and dysfunction. *Neuron* vol. 82 24–45 (2014).
32. Hong, T. T. *et al.* BIN1 localizes the L-type calcium channel to cardiac T-tubules. *PLoS Biol.* **8**, (2010).
33. Plumbly, W., Brandon, N., Deeb, T. Z., Hall, J. & Harwood, A. J. L-type voltage-gated calcium channel regulation of in vitro human cortical neuronal networks. *Sci. Rep.* **9**, (2019).
34. Green, E. M., Barrett, C. F., Bultynck, G., Shamah, S. M. & Dolmetsch, R. E. The Tumor Suppressor eIF3e Mediates Calcium-Dependent Internalization of the L-Type Calcium Channel CaV1.2. *Neuron* **55**, 615–632 (2007).
35. Vossel, K. A. *et al.* Seizures and Epileptiform Activity in the Early Stages of Alzheimer Disease. *JAMA Neurol.* **70**, 1158–1166 (2013).
36. Vossel, K. A., Tartaglia, M. C., Nygaard, H. B., Zeman, A. Z. & Miller, B. L. *Review Epileptic activity in Alzheimer's disease: causes and clinical relevance*. vol. 16 www.thelancet.com/neurology (2017).
37. Lam, A. D. *et al.* Silent hippocampal seizures and spikes identified by foramen ovale electrodes in Alzheimer's disease. *Nat. Med.* **23**, 678–680 (2017).
38. Turrigiano, G. G. & Nelson, S. B. Homeostatic plasticity in the developing nervous system. *Nat. Rev. Neurosci.* **5**, 97–107 (2004).
39. Frere, S. & Slutsky, I. Alzheimer's Disease: From Firing Instability to Homeostasis Network Collapse. *Neuron* vol. 97 32–58 (2018).
40. Dörrbaum, A. R., Alvarez-Castelao, B., Nassim-Assir, B., Langer, J. D. & Schuman, E. M. Proteome dynamics during homeostatic scaling in cultured neurons. *Elife* **9**, (2020).
41. Bezprozvanny, I. & Mattson, M. P. Neuronal calcium mishandling and the pathogenesis of Alzheimer's disease. *Trends Neurosci.* **31**, 454–463 (2008).

453 42. Carvalho, L. I., Lambert, J.-C. & Costa, M. R. Analysis of modular gene co-expression
454 networks reveals molecular pathways underlying Alzheimer's disease and progressive
455 supranuclear palsy. *medRxiv* 2021.09.21.21263793 (2021)
456 doi:10.1101/2021.09.21.21263793.
457 43. Ou, Y. N. *et al.* Genetically determined blood pressure, antihypertensive medications,
458 and risk of Alzheimer's disease: a Mendelian randomization study. *Alzheimer's Res.*
459 *Ther.* **13**, 1–9 (2021).
460 44. Wu, C. L. & Wen, S. H. A 10-year follow-up study of the association between calcium
461 channel blocker use and the risk of dementia in elderly hypertensive patients. *Med.*
462 *(United States)* **95**, (2016).
463
464

Figure legends

Figure 1: Transcriptional changes in BIN1 KO hiNs. (A) Immunohistochemistry for GFAP (red), MAP2 (green) and DAPI (blue) in 6.5-month-old *BIN1* WT and KO COs. (B) Western blots showing the isoforms of BIN1 detected in WT and the absence of BIN protein in KO COs. (C) UMAP representation of the different cell subtypes in COs identified using snRNA-seq. (D) Dot plot representing the expression for *BIN1* and key markers used to annotate cell subtypes. (E) Proportion of cell subpopulations in both genotypes (****p<0.0001; Chi-squared test). (F) Volcano plots representing DEGs comparing KO vs WT in astrocytes and glutamatergic neurons. DEGs with adjusted p-value <0.05 and |log2FC| >0.25 are shown in red. Gene labels are shown for top 10 genes in terms of log2FoldChange and p-value. (G) Functional enrichment analysis of DEGs identified in glutamatergic neurons. Bar plots representing the top 10 enriched gene ontology (GO) terms in biological processes (BP), cellular components (CC) and molecular function (MF) at p_{adj}<0.01. (H) Images showing *BIN1* WT and KO hiNs 7 days after the beginning of doxycycline treatment immunolabeled for neuronal markers MAP2 and TUBB3 and astrocyte marker GFAP and stained with DAPI. (I) UMAP representation of the different cell subtypes identified in ASCL1-hiNs cultures using snRNA-seq. (J) Dot plot representing expression of key markers used to annotate cell subtypes. (K) Volcano plot representing DEGs comparing *BIN1* KO vs WT glutamatergic neurons. DEGs with adjusted p-value <0.05 and |log2FC| >0.25 are shown in red. Gene labels are shown for calcium- and synapse-related genes. (L) Functional enrichment analysis of DEGs identified in glutamatergic neurons. Bar plots representing the top 10 enriched GO terms in each category at p_{adj}<0.01.

Figure 2: Similar molecular alterations in *BIN1* KO hiNs and glutamatergic neurons of the AD brain. (A) Box plot representing *BIN1* mRNA in expression through different Braak stages in entorhinal cortex (EC) and superior frontal gyrus (SFG) (***p_{adj}<0.001; Wilcoxon test). (B) Dot plot representing the overlap between DEGs identified in glutamatergic neurons of the AD brain and *BIN1* KO ASCL1-hiN cultures (left) or *BIN1* KO COs (right). (C-D) Network representation of enriched GO terms in overlapping DEGs between AD brains and glutamatergic neurons in culture. Enriched GO terms were identified using over-representation test. (E) Western blot for total TAU protein C-terminal (TAU-C), phosphorylated (p)-TAU at Ser202, Thr205 (AT8) and β-ACTIN in 4-week-old ASCL1-hiNs

cultures. (F) Quantification of TAU-C/β-ACTIN and p-TAU/TAU-C levels in BIN1 KO ASCL1-hiNs normalized to WT (*p=0.0262; Mann-Whitney test). (G) Western blot for total TAU protein C-terminal (TAU-C), phosphorylated (p)-TAU at Ser202, Thr205 (AT8) and β-ACTIN in 6.5month-old COs. (H) Quantification of TAU-C/β-ACTIN and p-TAU-TAU-C levels normalized to WT (*p=0.0357; #p=0.0714; Mann-Whitney test).

Figure 3: Similar synaptic density in *BIN1* WT and KO ASCL1-hiNs. (A-B) Immunocytochemistry using the astrocyte marker GFAP, neuronal marker MAP2, pre-synaptic marker SYP and post-synaptic marker HOMER1 in *BIN1* WT ASCL1-hiNs after 4 weeks of differentiation in a three-chamber microfluidic device. Scale bar = 200 µm. Rectangular box in A is magnified in B, allowing the identification of putative synaptic contacts (B'). (C-D) Fraction of SYP spots assigned by HOMER1 spots in MAP2 processes at 4 and 6 weeks ASCL1-hiNs cultures (n= 8 independent devices for each genotype). (E) Immunohistochemistry for HOMER1 (red), SYP (green) in 6.5-month-old *BIN1* WT and KO COs. (F) Quantifications of the number of SYP and HOMER1 spots, and the percentage of SYP assigned by HOMER1 spots in *BIN1* WT and KO COs (**p=0.0076; ***p=0.0002; Mann-Whitney test; n=3 COs per genotype).

Figure 4: Disorganization of neuronal activity in *BIN1* KO ASCL1-hiNs. (A) Raster plots showing the decomposition of multi-unity activity (MUA, black lines) into single-unit activity (SUA, colored lines) using spike waveform clustering. (B-E) Quantification of single-neuron firing rate (B; **p=0.0034), spike amplitude (C; *p=0.0106), burst duration (D; ****p<0.0001) and number of spikes per burst (E; ****p<0.0001) at 4 weeks. Mann-Whitney test; n= 5 independent experiments; WT: 376 neurons; KO: 416 neurons). (F) Raster plots showing SUA recorded from 5 different electrodes of *BIN1* WT (left) or KO (right) ASCL-hiNs cultures after 4 weeks of differentiation. (G) Array-wide spike detection rate (ASDR) plots based on SUA recorded in *BIN1* WT and KO ASCL1-hiNs cultures. Each line represents one independent culture batch. (H-I) Normalized autocorrelogram heatmap (H, each line refers to one SUA) and averaged correlation (I) for all SUAs recorded in 5 independent *BIN1* WT and KO ASCL1-hiNs cultures. (J) Percentage of spikes outside of bursts (*p=0.0417, Mann-Whitney test).

Figure 5: Altered electrical activity in *BIN1* KO COs. (A) Representative raster plots showing detected spikes in 5-month-old *BIN1* WT and KO COs recorded in a multi-well MEA device. (B) Spike frequency in Hz (**p=0.0068; Mann-Whitney test; n=4 WT and 3 KO COs). (C) Scheme indicating the different sets of ARGs regulated by brief and sustained patterns of electrical activity[28,29]. rPRGs: rapid primary response genes; dPRGs: delayed primary response genes; SRGs: secondary response genes; ERGs: early response genes; LRGs: late response genes; Exc – glutamatergic neurons; Inh – GABAergic neurons. (D) Feature plots showing the enrichment score of single cells for ARG signatures. Enrichment scores correspond to the $-\log10(p_{adj})$ of the Cell-ID-based enrichment test. (E) Proportions of glutamatergic (left) and GABAergic neurons (right) enriched for the different ARG signatures according to genotype (*p<0.05; ***p<0.001; Chi-squared test).

Figure 6: Altered frequency of calcium transients in *BIN1* KO ASCL1-hiNs. (A) Snapshot of a 4-week-old ASCL1-hiNs culture labeled with Oregon green BAPTA. (B) Representative plot of fluorescence change over time in 1000 frames. (C) Representative traces showing the fluorescence changes in *BIN1* WT and KO ASCL1-hiNs. Red dashed lines indicate the time to reach the fluorescence maximal intensity (raising time - t1) and to return to baseline (recovery time - t2). (D) Quantification of calcium transients in *BIN1* WT and KO ASCL1-hiNs (****p<0.0001; Mann-Whitney test; n= 3 independent cultures for each genotype; number of active cells per condition: 754 (WT), 1006 (KO)). (E-F) Quantification of rising time (t1) and recovery time (t2) for calcium transients (**p=0.0022; ****p<0.0001; Mann-Whitney test). (G) Images showing PLA spots using anti-BIN1 and anti-$Cav_{1.2}$ antibodies in 4-week-old *BIN1* WT and KO hiNs. Cells were also immunolabeled for the neuronal marker MAP2 (green), the astrocyte marker GFAP (white), and stained with DAPI (blue). (H) Western blot for Cav1.2 (without and with blocking peptide) and β-ACTIN in 4-week-old ASCL1-hiNs cultures. (I) Quantification of Cav1.2/β-ACTIN levels in *BIN1* WT and KO ASCL1-hiNs cultures ($^{\&}$p=0.0585; $^{\#}$p=0.0217; *p=0.0286; Unpaired t-test). (J) Western blot for $Cav_{1.2}$ and β-ACTIN in the total protein extracts from 4-week-old ASCL1-hiNs treated with KCl (+) or vehicle (-). Plot shows the quantification of $Cav_{1.2}$ normalized by β-ACTIN. (K) Western blot for $Cav_{1.2}$, $Cav_{1.3}$ and EEA1 in the endosomal protein extracts from 4-week-old ASCL1-hiNs treated with KCl (+) or vehicle (-). Plot shows the optical density of these proteins (****p<0.0001; Chi-square test). (L) Auto-correlograms of 4-week-old *BIN1* WT and KO hiNs treated or not with 50 nM

Nifedipine for 2 weeks. (M) Percentage of spikes outside of bursts (WT vs WT+NIF: **p_{adj}=0.0034; WT vs KO: *p_{adj}=0.0124; Dunn's multiple comparison test). (N) Average firing rates.

Supplementary data

Sup. Figure 1: Figure 1: Transcriptional changes in BIN1 HET COs. (A) Immunohistochemistry for GFAP (red), MAP2 (green) and DAPI (blue) in 6.5-month-old *BIN1* WT and HET COs. (B) Western blots showing the decrease in BIN1 expression in HET COs. (C) UMAP representation of the different cell subtypes in COs identified using snRNA-seq. (D) Cell proportions in each subpopulation in WT and HET COs. (E) Volcano plot representing DEG comparing HET vs WT in astrocytes and glutamatergic neurons. DEGs with adjusted p-value <0.05 and |log2FC| >0.25 are shown in red. Gene labels are shown for top 10 genes in terms of log2FoldChange and p-value. (F) Functional enrichment analysis of DEGs identified in *BIN1* HET glutamatergic neurons. Bar plots representing the top 10 enriched gene ontology (GO) terms in biological processes (BP), cellular components (CC) and molecular function (MF) at p_{adj}<0.01. (G) Venn diagram showing the overlap between DEGs identified in *BIN1* HET and KO glutamatergic neurons. (H) Bar plots representing the top 10 enriched GO:BP for common DEGs. (I) Immunohistochemistry for HOMER1 (red), synaptophysin (SYP, green) in 6.5-month-old *BIN1* WT and HET COs. (J) Quantification of the percentage of SYP assigned by HOMER1 spots in *BIN1* WT and HET COs (***p=0.0002; Mann-Whitney test; n=3 COs per genotype).

Sup. Figure 2: Transcriptional changes in spontaneously differentiated BIN1 KO hiNPCs. (A) UMAP representation of the different cell subtypes identified in 2D hiNPC cultures after 6 weeks of differentiation using snRNA-seq. (B) Proportion of cell subpopulations in both genotypes. (C) Dot plot representing expression of key markers used to annotate cell subtypes. (D) Volcano plot representing DEGs comparing *BIN1* KO vs WT glutamatergic neurons. DEGs with adjusted p-value <0.05 and |log2FC| >0.25 are shown in red. (E) Functional enrichment analysis of DEGs identified in glutamatergic neurons. Bar plots representing the top 10 enriched GO terms in each category at p_{adj}<0.01.

Sup. Figure 3: Normal APP processing in *BIN1* KO ASCL1-hiNs. (A) Western blots showing the expression of APP full-length, CTF-ß and ß-ACTIN at 4 weeks. (B) Quantification of the ratios APP/ß-ACTIN, CTF-ß/ß-ACTIN and CTF-ß/APP (n = 5 for each genotype). (C) Quantification of soluble $Aß_{1-x}$, $Aß_{1-42}$ and the ratio $Aß_{1-42/}$ $Aß_{1-x}$ in ASCL1-hiNs cultures at 3 and 4 weeks.

Sup. Figure 4: Normal glutamatergic transmission in *BIN1* KO ASCL1-hiNs. Box plots show the number of active spots per neuron and number of events detected by time-lapse video-microscopy in 4- or 6-week-old ASCL1-hiNs cultures transduced with the glutamate sensor iGLUSnFr (4 weeks: n= 378 BIN1 WT and 266 BIN1 KO ASCL1-hiNs; 6 weeks: n= 685 BIN1 WT and 629 BIN1 KO ASCL1-hiNs).

Sup. Figure 5: Increased spike burst frequency in *BIN1* KO ASCL-hiNs. (A) Bright-field image of ASCL1-hiNs cultures in microfluidic/MEA devices showing the cell chamber and micro channels. Neuron somata are mainly restricted to the cell chamber, whereas neuronal processes occupy microchannels. (B) Representative raster plots showing detected spikes in electrophysiological recordings of electrodes underneath the cell chamber and the micro channels, showing the higher sensitivity of the latter. (C) Raster plots showing MUA recorded for 1 minute in *BIN1* WT and KO ASCL1-hiNs after 4 weeks of differentiation. Each line represents one electrode localized side-by-side in our microfluidic/MEA array (as in panel A). (D-E) Quantification of the number of detected spikes at different time points (*p_{adj}=0.0141; ***p_{adj}=0.0006; Two-way ANOVA followed by Tukey's multiple-comparison test; n= 5 for each genotype). (F) Quantification of the number of spike bursts at different time points (**p=0.004; #p=0.0888; Mann-Whitney test).

Sup. Figure 6: Subtle increase in electrical activity in *BIN1* HET COs. (A) Representative raster plots showing detected spikes in 5-month-old *BIN1* WT and HET COs recorded in a multi-well MEA device. (B) Spike frequency in Hz (n=4 WT and 3 HET COs). (C) Proportions of glutamatergic neurons enriched for ARG signatures according to genotype (***p<0.001; Chi-squared test).

Sup. Figure 7: Expression of voltage-gated calcium channels in ASCL1-hiNs. (A) Violin plots showing the mRNA levels of Cav1 and Cav2 members of the voltage-gated calcium channel families L-type, P/Q-type, N-type and R-type detected in ASCL1 hiNs. (B) Images showing PLA spots using anti-BIN1 and anti-Cav1.3 antibodies in 4-week-old *BIN1* WT hiNs. Cells were also immunolabeled for the neuronal marker MAP2 (green), the astrocyte marker GFAP (white), and stained with DAPI (blue). (C) Western blots showing the expression of Cav1.3, Cav2.1, Cav2.2 and Cav2.3 in 4-week-old ASCL1h hiNs. (D) Quantification of protein expression.

Sup. Movies 1 and 2: Time-series of 1000 frames taken from *BIN1* WT and KO ASCL1-hiNs transduced with iGLUSnFr after 2 weeks of differentiation and imaged 2 weeks later. Videos are played at 100 fps.

Sup. Movies 3 and 4: Time-series of 1000 frames taken from *BIN1* WT and KO ASCL1-hiNs after 4 weeks of differentiation and labeled with Oregon Green BAPTA and imaged. Videos are played at 100 frames per second (fps).

Sup. Table 1: DEGs identified in different cell types/subtypes of COs.

Sup. Table 2: GO terms enriched for DEGs identified in different cell types/subtypes of COs.

Sup. Table 3: DEGs identified in different cell types/subtypes of ASCL1-hiNs cultures.

Sup. Table 4: GO terms enriched for DEGs identified in different cell types/subtypes of ASCL1-hiNs cultures.

Sup. Table 5: DEGs identified in different cell types/subtypes of the AD brain.

Sup. Table 6: GO terms enriched for DEGs commonly identified in *BIN1* HET or KO cells and the AD brain.

Sup. Table 7: List of ARGs used for Multiple Correspondence Analysis (MCA) in Cell-ID.

Online methods

Maintenance of cells and generation of hiNPCs and hiNs

hiPSCs modified for BIN1 in exon3 by CRISPR/Cas9 technology were sourced from Applied StemCell Inc. CA, USA. In addition to the BIN1 WT and KO hiPSCS, heterozygous (HET) iPSCS, harbouring a 1 bp insertion in one allele were also sourced Applied Stem Cells Inc. CA, USA.The parental cell line used for derivation of the cells was ASE 9109. The maintenance of these cells and the generation of hiNS, hiAs, and COs thereof, have been detailed in the publication by Lambert et al., 2022. All hiPSCs and their neuronal and glial cell derivatives including COs were maintained in media from Stemcell Technologies, Vancouver, Canada. Maintenance of cell cultures and COs were done following manufacturer's protocols which have been elucidated on the webpage of Stemcell Technologies. In addition, the embryoid body method detailed by Stemcell Technologies was used for the induction of BIN1 WT and KO hiPSCs. Cell numbers and viability were recorded using a LUNA™ Automated Cell Counter (Logos Biosystems, South Korea).

hiNs generated from ASCL1-transduced hiNPCs (protocol detailed in next section) were subjected to differentiation for 4 weeks. All differentiations were performed in tissue in 24-well cell imaging plates (0030741005, Eppendorf) culture dishes pre-coated with Poly-L-ornithine (P4957, Sigma-Aldrich) and Mouse Laminin (CC095, Sigma-Aldrich).

Differentiation protocol for induced hiNPCs

We differentiated neurons from virus-transduced hiNPCs according to an adapted protocol (Zhang et al., 2013; Yang et al., 2017). Briefly, hiNPCs are first transfected with the

TTA lentiviral construct and a passage later, the TetO-Ascl1-Puro lentiviral construct was transduced. These cells are maintained in NPM medium and expanded prior to differentiation. For differentiation of hiNs, hiNPCs are plated onto PLO/laminin-coated imaging plates at density 100,000 cells/well in NPM. After 24h, complete BrainPhys medium (BP) is added 1:1 together with 2 µg/mL doxycycline (Sigma-Aldrich) to induce TetO gene expression. The following day, 1 µg/mL puromycin (Sigma-Aldrich) was added to start cell selection. After 2-3 days (depending on the efficiency of antibiotic selection), 50,000 human cortical astrocytes were added in each well with BrainPhys containing doxycycline. After 24 hours, 2 µM of Ara-C (Cytosine β-D-arabinofuranoside) (Sigma-Aldrich) was added to arrest the proliferation of astrocytes. Half of the medium in each well was changed biweekly with fresh BrainPhys medium (StemCell Technologies) containing doxycycline until the 14th day. After that, the biweekly medium change was performed only with BrainPhys. Differentiation was allowed to continue for another 2 weeks prior to subjecting the cells to various experimental manipulations.

Human cortical astrocytes (Catalog # 1800) were sourced from ScienCell Research Laboratories, CA, USA. Maintenance and proliferation of astrocytes were done as per specifications mentioned on the datasheet from the provider which is available on their webpage.

This culture system was characterized using snRNA-seq showing that 70% of cells (n=3114 from 2 independent culture batches) expressed the pan-neuronal markers SOX11, SNAP25, DCX and RBFOX3, with 66% of cells co-expressing the glutamatergic neuron marker SLC17A6, less than 1.5% of cells co-expressing the GABAergic neuron markers DLX1, GAD1 and GAD2, and 5% of cells co-expressing low levels of markers of both neuronal subtypes. The remaining cells, immature astrocytes (Astro-I), mature astrocytes (Astro-II) and undifferentiated NPCs, represented about 15%, 8%, 4% of the cells, respectively. The first two cell populations likely represent two different states of astrocytes added to the cultures, whereas NPCs are likely cells that failed to reprogram into hiNs despite ASCL1 transduction.

Culture of Induced Neurons (hiNs) in Microfluidic Devices

Preparation of Microfluidic Devices: Three-compartment microfluidic neuron culture devices were used in which the presynaptic and postsynaptic chambers are connected to

719 the synaptic chamber by respectively long and short micro-channels. Details of the
720 microfluidic device design and fabrication have been previously described (Kilinc et al,
721 2020).

722 The homemade devices were placed individually in Petri dishes for easy handling and
723 UV sterilized for 30 min before coating for cell adhesion. The primary surface coating
724 consisted of poly-L-lysine (Sigma-Aldrich) at 20 µg/mL in borate buffer (0.31% boric acid,
725 0.475% sodium tetraborate, pH 8.5). All coated devices were incubated overnight at 37°C,
726 5% CO2. After a wash with DPBS, devices were then coated with 20 µg/mL laminin in DPBS
727 and incubated overnight at 37°C in 5% CO2. The following day, devices were carefully
728 washed once with DPBS before cell plating.

729 Cell Culture: In total, 30,000 NPCs resuspended in complete Neural Progenitor
730 Medium (NPM, Stemcell Technologies) containing 10 µM of Y-27632 ROCK inhibitor were
731 seeded per device, half at the entrance of the presynaptic somatic chamber and half at the
732 entrance of the postsynaptic somatic chamber. Microfluidic devices were microscopically
733 checked at the phase contrast to ensure the cells were correctly flowing into chambers.
734 After a minimum of 5 minutes to allow the cells to attach, devices were filled with NPM
735 (containing 10 µM of Y-27632 ROCK Inhibitor). Water was added to the Petri dishes to
736 prevent media evaporation, and these were then incubated at 37°C in a humidified 5% CO2
737 incubator. The spontaneous neuronal differentiation of NPCs started 24 hours later,
738 initiated by half medium change with complete BrainPhys Neuronal Medium. Induced
739 neuron cultures were maintained for 4 to 6 weeks with half of the medium replaced
740 biweekly with BrainPhys medium.

741 For induced neuron culture from NPCs transduced for Ascl1, doxycycline (2 µg/mL)
742 was added on the first day of half medium change to induce TetO gene expression. The
743 following day, puromycin (1 µg/mL) was added to start cell selection. Two days after the
744 puromycin selection, a total of 5,000 human cortical astrocytes (ScienCell Research
745 Laboratories, CA, USA) were added per device. After 24 hours, Ara-C (2 µM) was added to
746 stop their proliferation. Half of the medium was changed twice a week with complete
747 BrainPhys medium + 2 µg/mL doxycycline for 14 days. After that, half medium change was
748 performed only with BrainPhys medium.

749 Four microfluidic devices were employed for each experimental condition (*BIN1* KO vs
750 WT both for spontaneous neuronal differentiation and Ascl1 induction) and two

751 independent cultures were performed. To assess the time-course effect, neuron cultures
752 were stopped at 4 and 6 weeks.
753
754 *Generation of Cerebral Organoids*
755 Cerebral organoids (3D Cultures) were generated from wild-type, heterozygous and
756 knockout hiPSCs using a 4-stage protocol (Lancaster et al., 2013). The first step was the
757 Embryoid Body (EB) Formation Stage, where hiPCSc at 80%-90% confluency were detached
758 from the Vitronectin XF substrate using Accutase (#AT-104, Innovative Cell Technologies). To
759 form the EB, 9000 cells were plated per well in a 96-well round-bottom ultra-low
760 attachment plate containing EB seeding medium (Stem Cell Technologies). After two days,
761 the EBs were transferred to a 24-well ultra-low attachment plate containing Induction
762 Medium (Stem Cell Technologies), where each well receives 1-2 EBs. This was the Induction
763 Stage. Two days later, the EBs were ready for the Expansion Stage. The EBs were embedded
764 in Matrigel (Corning) and transferred to a 24-well ultra-low adherent plate with Expansion
765 Medium (Stem Cell Technologies). After three days, the medium was replaced by
766 Maturation Medium (Stem Cell Technologies) and the plate was placed in an orbital shaker
767 (100 rpm speed). During this final Maturation Phase, 75% medium change was done on a
768 biweekly basis. Organoids were allowed to mature for a period of 6.5 months.
769
770 *Viral Transductions*
771 Lentiviral constructs were produced by the Vect'UB platform within the TBM Core unit
772 at University of Bordeaux, Bordeaux, France (CNRS UMS 3427, INSERM US 005). The
773 lentiviral constructs used were TTA (ID # 571) and TetO-Ascl1-Puro (Addgene, Plasmid #
774 97329). Lentiviral infections were done in NPCs at P3 or P4. The viral constructs were
775 transduced at a multiplicity of infection (MOI) of 2.5. In brief, NPCs were plated at a
776 confluency of 1x106 cells per well of a 6-well plate. After 4 hours of plating the cells,
777 appropriate volumes of each lentiviral construct were mixed in complete Neural Progenitor
778 medium and 50 µl of the viral medium mix was then added to each well. We transduced the
779 TTA construct at first in the NPCs. Following one passage, the TTA-transduced cells were
780 transduced with the construct for Ascl1. Cells having both viral constructs were then further
781 expanded for 1 or 2 passages before being used for differentiation into hiNs.

The iGluSnFR construct was an adeno-associated viral vector (BS11-COG-AAV8) sourced from Vigene Biosciences, MD, USA. The viral construct was transduced at a MOI of 5,000 at around 10 days of differentiation for the ASCL1-hiNs. Differentiation was allowed to continue for a duration of 4 weeks prior to imaging.

Immunocytochemistry and Immunohistochemistry

Bidimensional (2D) cultures: All cells were fixed in 4% (w/v) paraformaldehyde (Electron Microscopy Sciences, Catalog # 15712) for 10 minutes in the imaging plates. Following, fixation, cells were washed thrice with PBS 0.1 M. Blocking solution (5% normal donkey serum + 0.1% Triton X-100 in PBS 0.1 M) was added to fixed cells at room temperature for 1 hour under shaking conditions. After the blocking step, primary antibodies were added to cells in the blocking solution and incubated overnight at 4°C. The following day, cells were washed with PBS 0.1 M thrice for 10 mins. Each. Alexa Fluor®--conjugated secondary antibodies in blocking solution were then incubated with the cells for 2 hours at room temperature under shaking conditions ensuring protection from light. Subsequently, 3 washes with 0.1 M PBS were done for 10 min each at room temperature under shaking conditions with protection from light. Hoechst 33258 solution was added during the second PBS wash. Cells were mounted with Aqua-Poly/Mount (Polysciences, Inc.) and imaged directly in the cell imaging plates. All images were acquired using an LSM 880 Confocal Scanning Microscope housed at the Imaging Platform of the Pasteur Institute, Lille. Duolink® Proximity Ligation Assays (PLA) was used to detect endogenous Protein-Protein Interactions. The following pairs of antibodies were used: anti-BIN1 (rabbit, 182562, abcam) and anti-Cav1.2 (mouse, 84814, abcam); or anti-BIN1 and anti-Cav1.3 (mouse, 85491, mouse). Other antibodies used for immunocytochemistry were: MAP2 (188006 and 188004, Synaptic Systems), Beta III Tubulin (MAB1637, Sigma-Aldrich), GFAP (AB5804, Millipore; and 173006, Synaptic Systems). All Alexa Fluor®-tagged secondary antibodies were sourced from Jacskon ImmunoResearch Europe Ltd.

Microfluidic Devices: Cultured induced neurons were fixed in 4% paraformaldehyde in PBS for 15 min at room temperature, washed three times with PBS, and permeabilized with 0.3% Triton X-100 in PBS for 5 min at room temperature. Cells were blocked in PBS containing 5% normal donkey serum for 1 h at room temperature before overnight incubation at 4°C with the following primary antibodies: MAP2 (188006, Synaptic Systems);

HOMER1 (160004, Synaptic Systems), Synaptophysin (101011, Synaptic Systems), and GFAP (AB5804, Millipore). Cells were washed twice with PBS and incubated with the following secondary antibodies for 2h at room temperature: DyLight™ 405 Donkey Anti-Chicken (703-475-155, Jackson ImmunoResearch), Alexa Fluor 594 Donkey Anti-Guinea Pig (706-585-148, Jackson ImmunoResearch), Alexa Fluor 488 Donkey Anti-Mouse (715-545-151, Jackson ImmunoResearch) and Alexa Fluor 647 Donkey Anti-Rabbit (711-605-152, Jackson ImmunoResearch). Cells were rinsed three times with PBS and microfluidic devices were mounted with 90% glycerol.

Samples were imaged with a LSM 880 confocal microscope with a 63X 1.4 NA objective. Images were acquired at zoom 2 in z-stacks of 0.5 µm interval. Typically, 6 images were acquired per device from the synapse chamber near the postsynaptic chamber such the image contains multiple dendrites. Images were deconvoluted using the Huygens software (Scientific Volume Imaging, Netherlands).

Cerebral Organoids: Cerebral organoids were fixed in 4% PFA (w/v) for 30 min at 4°C followed by three washes with PBS 0.1 M. Cerebral organoids were then placed in sucrose solution (30% w/v) overnight before being embedded in O.C.T (Tissue-Tek). Embedded tissue was sectioned at 20 µm using a Cryostar NX70 Cryostat (Thermo Scientific) and mounted slides were stored at −80°C until immunostaining was performed. For immunostaining, tissue sections were brought to room temperature and then rehydrated with 3 washes with 0.1 M PBS, each for 5 mins. Slides were then washed once with PBS with 0.2% Triton X-100 for 15 mins. Tissue was blocked using 10% of donkey serum in PBS 0.1 M for 1 h at room temperature. After blocking, primary antibodies were added to 0.2 % Triton X-100 and 10% of donkey serum in PBS 0.1 M at appropriate dilutions and incubated overnight at 4°C. The next day, slides were washed with PBS 0.1 M 3 times for 5 min each with gentle shaking. Subsequently, slides were incubated with Alexa Fluor®-conjugated secondary antibodies in 0.2 % Triton X-100 and 10% of donkey serum in PBS 0.1 M for 2 h at room temperature in the dark. After secondary antibody incubation, slides were washed 3 times with PBS for 5 min with gentle shanking. Nuclei were visualized by incubating the tissue for 5 min with Hoechst 33258 stain in PBS 0.1 M. Sections were mounted using aqueous mounting medium (Polysciences). Images were acquired using an LSM 880 Confocal Scanning Microscope in concert with the ZEISS ZEN imaging software housed at the Imaging Platform of the Pasteur Institute, Lille. Image acquisition was done at 40X for the

various cellular markers in Fig. 1. The antibodies used were MAP2 (188006, Synaptic Systems) and GFAP (AB5804, Sigma-Aldrich).

Quantification of Synaptic Connectivity

Synaptic connectivity was quantified as previously described (Kilinc et al, 2020). Briefly, images were analyzed with Imaris software (Bitplane, Zürich, Switzerland) by reconstructing Synaptophysin I and HOMER1 puncta in 3D. The volume and position information of all puncta were processed using a custom Matlab (MathWorks, Natick, MA) program. This program assigns each postsynaptic spot to the nearest presynaptic spot (within a distance threshold of 1 µm) and calculates the number of such assignments for all presynaptic puncta.

Immunoblotting

Samples from the 2D cultures or brain organoids were collected in RIPA buffer containing protease and phosphatase inhibitors (Complete mini, Roche Applied Science) and sonicated several times at 60%-70% for 10 seconds prior to use for the immunoblotting analyses. Protein quantification was performed using the BCA protein assay (ThermoFisher Scientific). 10 µg of protein from extracts were separated in NuPAGE 4-12% Bis-Tris Gel 1.0mm (NP0321BOX, Thermo Scientific) or 3-8% Tri-Acetate gel (EA03755BOX, Thermo Scientific) and transferred on to nitrocellulose membranes 0.2µm (#1704158, Bio-Rad). Next, membranes were incubated in milk (5% in Tris-buffered saline with 0.1% Tween-20 (TBST)) or SuperBlock (37536, ThermoFisher Scientific) to block non-specific binding sites for 1 hour at room temperature, followed by several washes with TBST 0.1% or TNT 1x as washing buffers. Immunoblottings were carried out with primary antibodies overnight at 4°C under shaking condition. The membranes were washed three times in the washing buffer, followed by incubation with HRP-conjugated secondary antibodies for 2 hours at room temperature under shaking condition. The membranes were washed three times in washing buffer, and the immune reactivity was revealed using the ECL chemiluminescence system (SuperSignal, ThermoScientific) and imaged using the Amersham Imager 600 (GE Life Sciences). Optical densities of bands were quantified using the Gel Analyzer plugin in Fiji–ImageJ. The primary antibodies used for the immunoblots were as follows: BIN1 (ab182562,Abcam), APP C-terminal (A8717, Sigma-Aldrich), Tau (A002401-2, Agilent)

878 Phospho-Tau(Clone: AT8) (MN1020,ThermoFisher Scientific), CaV1.3 (CACNA1D) (ACC-005,
879 Alomone), CaV2.1 (CACNA1A) (ACC-001, Alomone), CaV2.2 (CACNA1B) (ACC-002, Alomone),
880 CaV2.3 (CACNA1E) (ACC-006, Alomone), CaV1.2 (CACNA1C) (AGP-001 and ACC-003,
881 Alomone), blocking peptide for Anti-CaV1.2 (CACNA1C) (BLP-CC003, Alomone) and β-ACTIN
882 (A1978, Sigma-Aldrich). Secondary antibodies used for the immunoblots were Mouse-HRP
883 (115-035-003, Jackson ImmunoResearch), Rabbit-HRP (111-035-003, Jackson
884 ImmunoResearch), and Guinea pig-HRP (106-035-003, Jackson ImmunoResearch).
885
886 *Activity-dependent endosytosis assay*
887 ASCL1-hiNs (n=9 cultures from each genotype) were subjected to 30 min of
888 depolarization with 65 mM KCl or a mock treatment. Cells were then collected and pulled
889 for endosomal fraction purification using the Minute™ Endosome Isolation and Cell
890 Fractionation Kit (Invent Biotechnologies). Western blot was performed as described above.
891
892 *AlphaLISA measurements*
893 Cell culture media samples for AlphaLISA measurements were collected at the endof
894 the 3rd and 4th weeks of differentiation of the ASCL1-hiNs. Alpha-LISA kits specific for
895 human Aβ1–X (AL288C, PerkinElmer) and Aβ1–42 (AL276C, PerkinElmer) were used to
896 measure the amount of Aβ1–X and Aβ1–42 respectively in culture media. The human Aβ
897 analyte standard was diluted in the BrainPhys medium. For the assay, 2 µL of cell culture
898 medium or standard solution was added to an Optiplate-384 microplate (PerkinElmer). 2 µL
899 of 10X mixture including acceptor beads and biotinylated antibody was then added to the
900 wells with culture media or standard solution. Following incubation at room temperature
901 for an hour, 16 µL of 1.25X donor beads was added to respective wells and incubated at
902 room temperature for 1 hour. Luminescence was measured using an EnVision-Alpha Reader
903 (PerkinElmer) at 680-nm excitation and 615-nm emission wavelengths.
904
905 *Calcium and iGluSnFR Imaging*
906 Calcium imaging was performed in 2D cultures after 4-weeks (Ascl1-induced). Prior to
907 imaging, the cells were incubated with Oregon Green™ 488 BAPTA-1 (OGB-1) acetoxymethyl
908 (AM) (ThermoFisher Scientific) for 1 hour. A 2.5 mM stock solution of the calcium-indicator
909 dye was prepared in Pluronic™ F-127 (20% solution in DMSO) (ThermoFisher Scientific). 1 µL

of the dye solution was added to 400 µL of fresh BrainPhys medium in each well of a 24-well cell imaging plate. Existing BrainPhys media from the wells of the plate was removed and kept aside while the calcium-indicator dye was incubated in fresh BrainPhys medium. After the 1-hour incubation, the medium which was kept aside was replaced to each well. The 2D cultures were then ready to be filmed using a Spinning Disk Microscope housed at the Institut Pasteur de Lille, Lille, France using the MetaMorph imaging software.

For filming the calcium activity, 1000 images were taken using a 20X long-distance objective, 10 ms exposure time and 200ms intervals. For each well, 5 random fields were chosen, and the cellular activity was, thus, recorded.

For cells transduced with iGluSnFR, these cells were directly filmed after 4 weeks of differentiation and 500 images were taken using a 20X long-distance objective, 10 ms exposure time and 200ms intervals. Up to 8 fields per well were filmed, each field containing at least one fluorescent transduced cell along with its processes.

Analyses of Calcium Transients

All live recordings of neuronal calcium transients were first converted into .avi format after background subtraction using the FIJI software. Following these, the videos were subsequently opened using the free software for data analyses of calcium imaging, CALciumIMagingAnalyzer (CALIMA) made available online by Fer Radstake (Eindhoven University of Technology, The Netherlands). Each video recording of a field of cells was first downscaled to 2X in terms of size with a 10X zoom and was checked for the frame average mode. Moreover, in this first detection stage, pre-set filter parameters were adjusted and applied to enable the detection of the maximum number of fluorescent cells in each field. In the analysis tab, detection of the average activity was checked and for pre-processing, a median of 3 was applied. All cells within the pre-set filter parameters are detected as regions of interest (ROIs) in the detection stage. Cell activity from all detected ROIs is then recorded. However, in the subsequent analysis stage, only cells showing spiking frequencies with a standard deviation of at least 2 or more were taken into consideration. Data in the form of detection spikes and the correlation (peak) are extracted and exported as CSV files.

Electrophysiological recordings in 2D cultures and cerebral organoids

ASCL1-hiNs were cultured in the aforementioned microfluidic devices bound to multi-electrode arrays (256MEA100/30iR-ITO, Multi-Channel Systems, Germany). Extracellular action potentials were recorded in 5 different cultures for both genotypes at 2, 3, 4 and 6 weeks of differentiation using the MEA2100-256-System (Multi-Channel Systems). Before recordings, MEAs were let stabilize for 5 min on the headstage to reduce artifacts due to medium movement. Signals were recorded for 1 min, at 40 kHz sampling rate, using Multi Channel Experimenter 2.16.0 software (Multi-Channel Systems). Electrical activity in cerebral organoids was recorded using 256-6wellMEA200/30iR-ITO (Multi-Channel Systems, Germany). Briefly, 5-6-month-old cerebral organoids were mounted onto MEAs and kept for 2 h in complete Brainphys medium. Then, MEAs were placed on the headstage and let stabilize for 5 min before recordings. Signals were recorded for 5 min, at 10 kHz sampling rate using Multi-Channel Experimenter 2.16.0. For rescue experiments using a calcium channel blocker, ASCL1-hiNs were cultured MEA 96-well plates (CytoView MEA 96, Axion Biosystems, USA). Extracellular action potentials were recorded in 3 independent cultures for either genotype in the presence of 50nM nifedipine (Tocris Bioscience) or vehicle using the MaestroPro (Axion Biosystems, Inc, USA). Before recordings, MEAs were let stabilize for 5 min on the MaestroPro at 37°C and 5% CO_2. Signals were recorded for 3 min, at 12.5 kHz sampling rate, using AxIS Navigator software (Axion Biosystems).

Spikes were detected using a fixed amplitude threshold of 5.5 and 4.5 standard deviations (for the 2D and 3D cultures, respectively) of the high-pass filtered (>300 Hz) signal for positive- and negative-going signals. The detection included a dead time of 3 ms to account for the refractory period of action potentials. Quantification of the number of detected spikes (MUAs) and spike bursts (defined as at least 5 spikes within 50 ms) was performed using Multi-Channel Analyzer 2.16.0 software (Multi-Channel Systems).

Spike sorting and temporal structure of spontaneous activity

Channels containing detected waveforms were manually processed offline for spike waveform separation and classification using Offline Sorter v3 (Plexon, USA). Briefly, we applied principal component analysis (PCA) to cluster spike waveforms of similar morphologies. Using this approach, we identified from 2 to 10 well-isolated units per channel, and therefore, we considered this single-unit activity (SUA). For each SUA, we computed the average firing rate, the signal-to-noise ratio, the peak-to-trough amplitude

and duration, the average power (square amplitude of the average waveform), the mode of the interspike interval distribution, and their firing patterns. It has been demonstrated that dissociated neuronal cultures can develop complex discharge structures (Wagenaar, 2006). Here, we considered burst activity if the SUA presents periods of high-frequency discharges interspersed by regular or no discharges at all. Operationally, a burst must have at least 3 spikes within 100 ms and 200 ms intervals, for the interval between the first and the second, and the second and the third discharge, respectively. After the third spike, the maximal interval to consider a discharge part of the burst was 200 ms. Thus, we computed the SUA that presented bursts, the number of bursts (i.e., the burst frequency), the average burst duration, the number of spikes within each burst, the average burst frequency, and the inter-burst interval.

Two complementary approaches investigated the temporal structures of spike trains. In the first one, we computed the array-wide spike detection rate (ASDR), which is the number of spikes detected per unit of time, summed over all electrodes in the array. This method is commonly used in the literature to demonstrate synchronous activity (aka, bursts) in MUA data (Wagenaar 2006). The second approach uses the autocorrelation function (i.e., the probability of finding two spikes at a given time interval) to calculate the oscillation score and the oscillation period of every single unit (Muresan 2008:1333, J Neurophysiol). Briefly, the oscillation score was calculated as the averaged absolute magnitude difference between the positive and negative peaks of the smoothed autocorrelation function (bin size of 200 ms). The oscillation period was calculated as the averaged time interval of the positive peaks of the autocorrelation function.

snRNA-seq Library Preparation

Nuclei isolation and Hash-tagging with oligonucleotides steps were realized on ice with pre-cold buffers and centrifugations at 4°C. 6.5-month-old BIN1 WT, HET, and KO organoids were processed as previously (Lambert et al., 2022). 4-week-old cultured ASCL1-induced BIN1 WT and KO 2D cultures were washed in the imaging plate wells with 500 µL of Deionized Phosphate Buffer Saline 1X (DPBS, GIBCO™, Fisher Scientific 11590476). Cells were resuspended with wide bore tips in 500 µL Lysis Buffer (Tris-HCL 10mM, NaCl 10mM, MgCl2 3mM, Tween-20 0,1%, Nonidet P40 Substitute 0,1%, Digitonin 0,01%, BSA 1%, Invitrogen™ RNAseout™ recombinant ribonuclease inhibitor 0,04 U/µL). Multiple

mechanical resuspensions in this buffer were performed for a total lysis time of 15 mins., 500 µL of washing buffer was added (Tris-HCL 10mM, NaCl 10 mM, MgCl2 3 mM, Tween-20 0.1%, BSA 1%, Invitrogen™ RNAseout™ recombinant ribonuclease inhibitor 0,04 U/µL) and the lysis suspension was centrifuged 8 mins. at 500 g (used for all following centrifugation steps). Nuclei pellets were washed tree times with one filtration step by MACS pre-separation filter 20µm (Miltenyi Biotec). Nuclei pellets were resuspended in 100 µL of staining buffer (DPBS BSA 2%, Tween-20 0.01%), 10 µL of Fc blocking reagent HumanTruStainFc™ (422302, Biolegend) and incubated 5 min at 4°C. 1µl of antibody was added (Total-Seq™-A0453 anti-Vertebrate Nuclear Hashtag 3 MAb414 for the WT and Total-Seq™-A0454 anti-Vertebrate Nuclear Hashtag 4 MAb414 for the KO, 97286 and 97287 respectively, Biolegend) and incubated 15 mins. at 4°C. Nuclei pellets were washed three times in staining buffer with one filtration step by MACS pre-separation filter 20 µm (Miltenyi Biotec) to a final resuspension in 300 µL of staining buffer for Malassez cell counting with Trypan blue counterstaining (Trypan Blue solution, 11538886, Fisherscientific). Isolated nuclei were loaded on a Chromium 10X genomics controller following the manufacturer protocol using the chromium single-cell v3 chemistry and single indexing and the adapted protocol by Biolegend for the HTO library preparation. The resulting libraries were pooled at equimolar proportions with a 9 for 1 ratio for Gene expression library and HTO library respectively. Finally, the pool was sequenced using 100pb paired-end reads on NOVAseq 6000 system following the manufacturer recommendations (Illumina).

snRNA-seq Dataset Preprocessing

Unique Molecular Index (UMI) Count Matrices for gene expression and for Hash Tag Oligonucleotide (HTO) libraries were generated using the CellRanger count (Feature Barcode) pipeline. Reads were aligned on the GRCh38-3.0.0 transcriptome reference (10x Genomics). Filtering for low quality cells according to the number of RNA, genes detected, and percentage of mitochondrial RNA was performed. For HTO sample, the HTO matrix was normalized using centered log-ratio (CLR) transformation and cells were assigned back to their sample of origin using HTODemux function of the Seurat R Package (v4)[10]. Then, normalizations of the gene expression matrix for cellular sequencing depth, mitochondrial

1036 percentage and cell cycle phases using the variance stabilizing transformation (vst) based
1037 Seurat:SCTransform function were performed.
1038
1039 *snRNA-seq datasets integration and annotation*
1040 To integrate the datasets from independent experiments, the harmony R package
1041 (https://github.com/immunogenomics/harmony) was used. In order to integrate the
1042 datasets, the SCTransform normalized matrices was merged and PCA was performed using
1043 Seurat::RunPCA default parameter. The 50 principal components (dimensions) of the PCA
1044 were corrected for batch effect using harmony::RunHarmony function. Then, the 30 first
1045 batch corrected dimensions were used as input for graph-based cell clustering and
1046 visualization tool. Seurat::FindNeighbors using default parameters and Seurat::FindClusters
1047 function using the Louvain algorithm were used to cluster cells according to their batch
1048 corrected transcriptomes similarities. To visualize the cells similarities in a 2-dimension
1049 space, the Seurat::RunUMAP function using default parameter was used. Cell clusters were
1050 then annotated based on cell type specific gene expression markers.
1051
1052 *Differential gene expression and GO enrichment analyses*
1053 Gene expression within each main cell type was compared between conditions of
1054 interest using Wilcoxon test on the SCTransform normalized gene expression matrix. GO
1055 enrichment analysis on the differentially expressed genes was performed using the gost
1056 function of the gprofiler2 R package (CRAN).
1057
1058 *Activity-related genes (ARGs) signature enrichment analysis at single cell resolution*
1059 To study enrichment for activity-related genes (ARGs) signature across cerebral
1060 organoid cells, the CellID R package (https://github.com/RausellLab/CelliD) was used. ARGs
1061 obtained from Tyssowski et al. (2018) and Hravtin et al. (2018) (supplementary Table 7),
1062 were translated to the corresponding human gene name with the help of the biomaRt
1063 package using the respective Ensembl references. Then, the CellID::RunMCA was used to
1064 extract cell-specific gene signature and hypergeometric test was performed to test
1065 enrichment for ARGs in these cell signatures. To test the differential proportion of ARGs
1066 enriched cells in BIN1 deleted organoid compared to WT organoid, chi-squared test was
1067 performed.

Comparative analysis with specific DEGs in AD brains

To compare the transcriptomic change observed in BIN1 deleted cerebral organoid with those observed in AD brain, datasets from the work of Leng et al. (ref) and Morabito et al. (ref) were taken as 2 independent references. The raw gene expression matrix was normalized using Seurat::SCTransform and differential expression analysis was performed within each neuronal cell type using Wilcoxon test as used for our organoid dataset. AD related DEGs, thus, obtained were compared with our BIN1 related organoid DEGs in every cell type. To this end, the enrichment for AD-related DEGs in BIN1-related DEGs was tested using hypergeometric test. The background for this test was defined as all genes detected in both datasets. The p-value of this test was used as metrics to compare the significance of the gene overlap between neuronal cell types.

Statistical analysis

Statistical analysis was performed using GraphPad Prism version 8.0.0 (GraphPad Software, San Diego, California USA, www.graphpad.com) and R 4.2.0 (R Core Team, 2022, https://cran.r-project.org/bin/windows/base/old/4.2.0/). Bar plots show mean ± SD and individual values. Box plots show 1-99 percentile. Statistical tests and p values are indicated in figure legends.

Figure 2

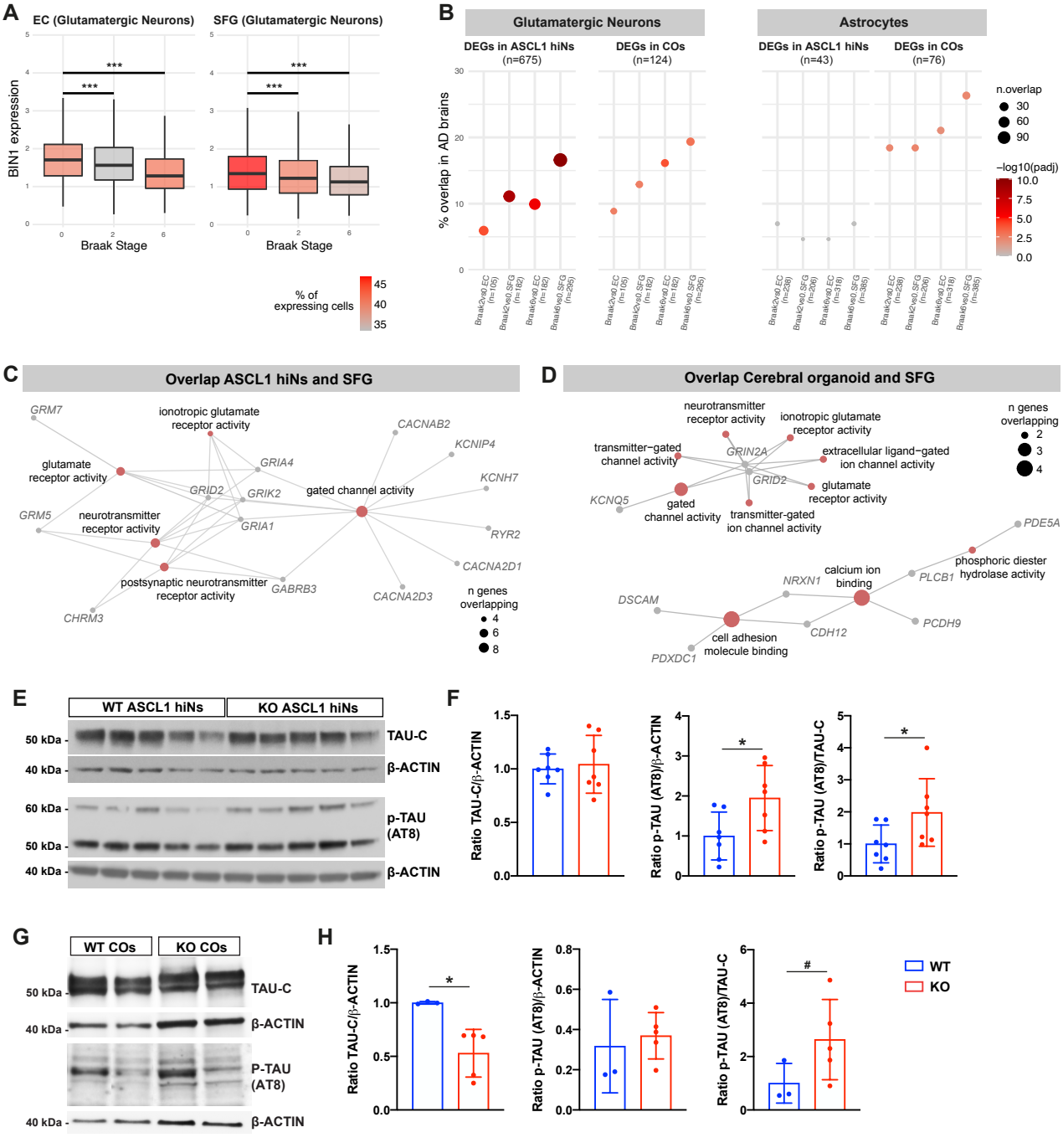
A
EC (Glutamatergic Neurons)
SFG (Glutamatergic Neurons)
BIN1 expression
Braak Stage
***
% of expressing cells
45
40
35
B
Glutamatergic Neurons
Astrocytes
DEGs in ASCL1 hiNs (n=675)
DEGs in COs (n=124)
DEGs in ASCL1 hiNs (n=43)
DEGs in COs (n=76)
% overlap in AD brains
n.overlap
30
60
90
−log10(padj)
10.0
7.5
5.0
2.5
0.0
C
Overlap ASCL1 hiNs and SFG
GRM7
ionotropic glutamate receptor activity
CACNAB2
KCNIP4
glutamate receptor activity
GRIA4
KCNH7
GRID2
GRIK2
gated channel activity
GRM5
neurotransmitter receptor activity
GRIA1
RYR2
CACNA2D1
postsynaptic neurotransmitter receptor activity
GABRB3
CACNA2D3
CHRM3
n genes overlapping
4
6
8
D
Overlap Cerebral organoid and SFG
neurotransmitter receptor activity
ionotropic glutamate receptor activity
n genes overlapping
2
3
4
transmitter−gated channel activity
GRIN2A
extracellular ligand−gated ion channel activity
GRID2
glutamate receptor activity
KCNQ5
gated channel activity
transmitter-gated ion channel activity
PDE5A
phosphoric diester hydrolase activity
PLCB1
NRXN1
calcium ion binding
DSCAM
PCDH9
CDH12
cell adhesion molecule binding
PDXDC1
E
WT ASCL1 hiNs
KO ASCL1 hiNs
50 kDa
40 kDa
TAU-C
β-ACTIN
60 kDa
50 kDa
40 kDa
p-TAU (AT8)
β-ACTIN
F
Ratio TAU-C/β-ACTIN
Ratio p-TAU (AT8)/β-ACTIN
Ratio p-TAU (AT8)/TAU-C
*
G
WT COs
KO COs
50 kDa
40 kDa
TAU-C
β-ACTIN
P-TAU (AT8)
40 kDa
β-ACTIN
H
Ratio TAU-C/β-ACTIN
Ratio p-TAU (AT8)/β-ACTIN
Ratio p-TAU (AT8)/TAU-C
*
#
WT
KO

Figure 3

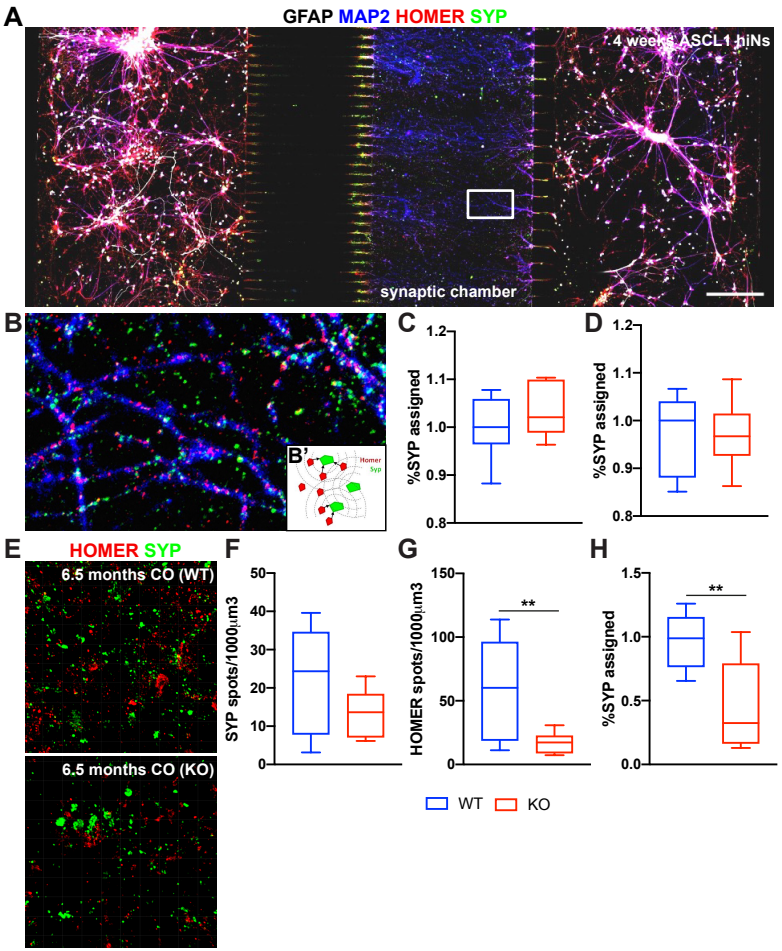
A
GFAP MAP2 HOMER SYP
4 weeks ASCL1 hiNs
synaptic chamber
B
B'
Homer
Syp
C
%SYP assigned
1.2
1.1
1.0
0.9
0.8
D
%SYP assigned
1.2
1.1
1.0
0.9
0.8
E
HOMER SYP
6.5 months CO (WT)
6.5 months CO (KO)
F
SYP spots/1000µm3
50
40
30
20
10
0
G
HOMER spots/1000µm3
150
100
50
0
**
H
%SYP assigned
1.5
1.0
0.5
0.0
**
WT
KO

Figure 4

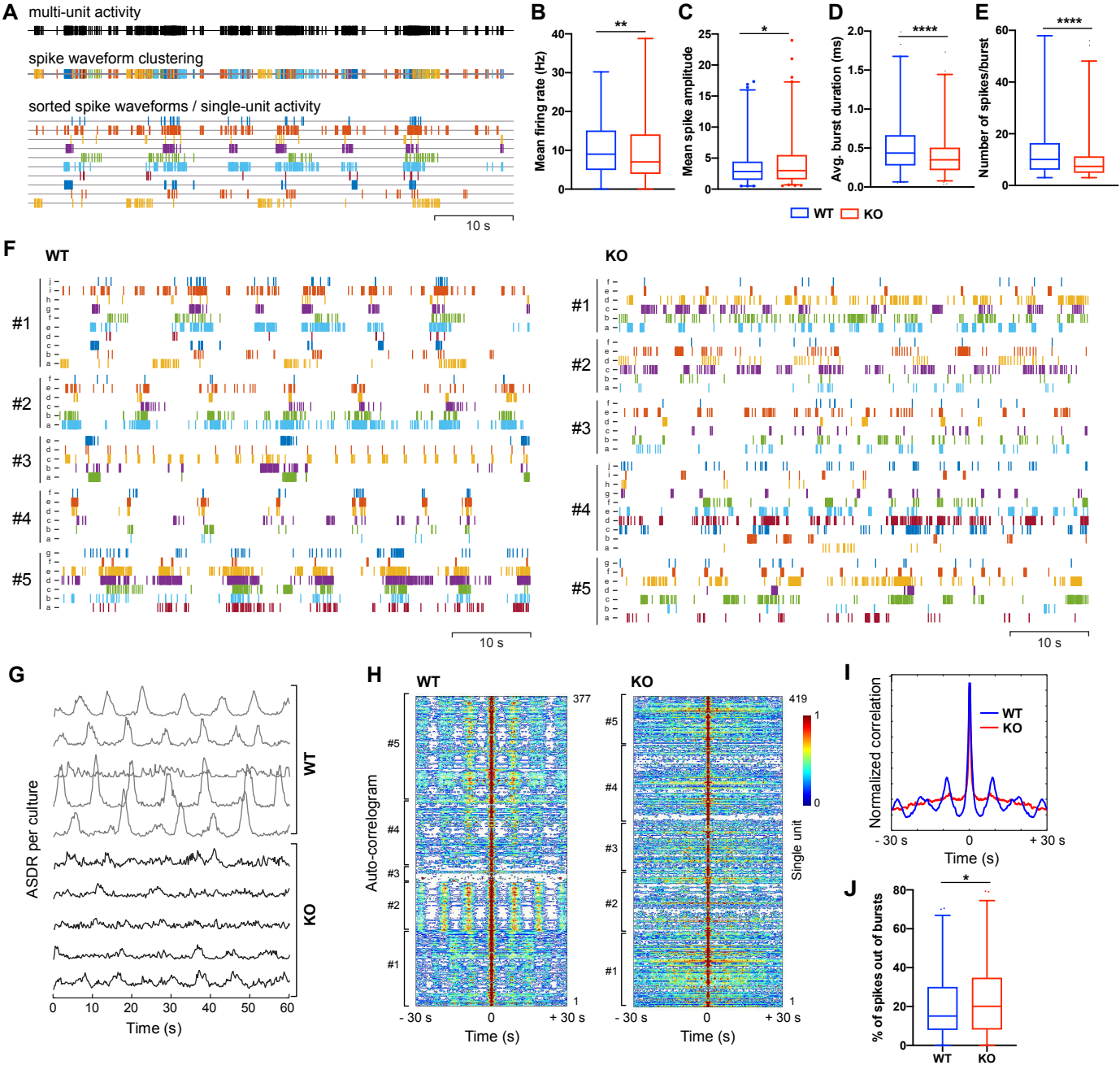
A
multi-unit activity
spike waveform clustering
sorted spike waveforms / single-unit activity
10 s
B
Mean firing rate (Hz)
**
C
Mean spike amplitude
*
D
Avg. burst duration (ms)
****
E
Number of spikes/burst
****
WT
KO
F
WT
KO
#1
#2
#3
#4
#5
10 s
G
ASDR per culture
WT
KO
Time (s)
H
WT
KO
Auto-correlogram
377
419
Single unit
- 30 s
0
+ 30 s
Time (s)
I
Normalized correlation
WT
KO
- 30 s
0
+ 30 s
Time (s)
J
% of spikes out of bursts
*
WT
KO

Figure 5

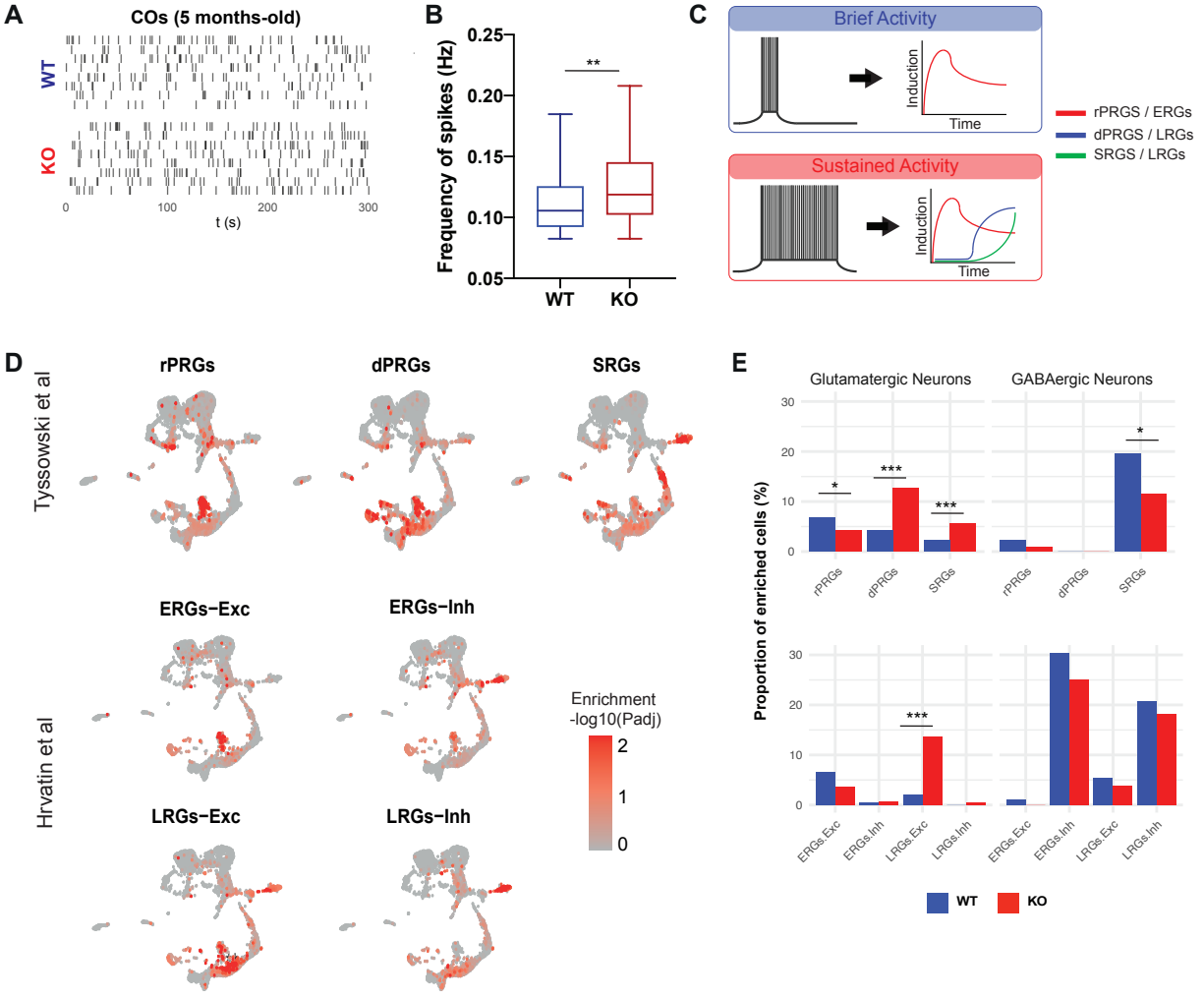
A
COs (5 months-old)
WT
KO
0
100
200
300
t (s)
B
Frequency of spikes (Hz)
0.25
0.20
0.15
0.10
0.05
**
WT
KO
C
Brief Activity
Induction
Time
Sustained Activity
Induction
Time
rPRGS / ERGs
dPRGS / LRGs
SRGS / LRGs
D
Tyssowski et al
Hrvatin et al
rPRGs
dPRGs
SRGs
ERGs−Exc
ERGs−Inh
LRGs−Exc
LRGs−Inh
Enrichment
-log10(Padj)
2
1
0
E
Glutamatergic Neurons
GABAergic Neurons
Proportion of enriched cells (%)
30
20
10
0
*
***
***
*
rPRGs
dPRGs
SRGs
ERGs.Exc
ERGs.Inh
LRGs.Exc
LRGs.Inh
WT
KO

Figure 1

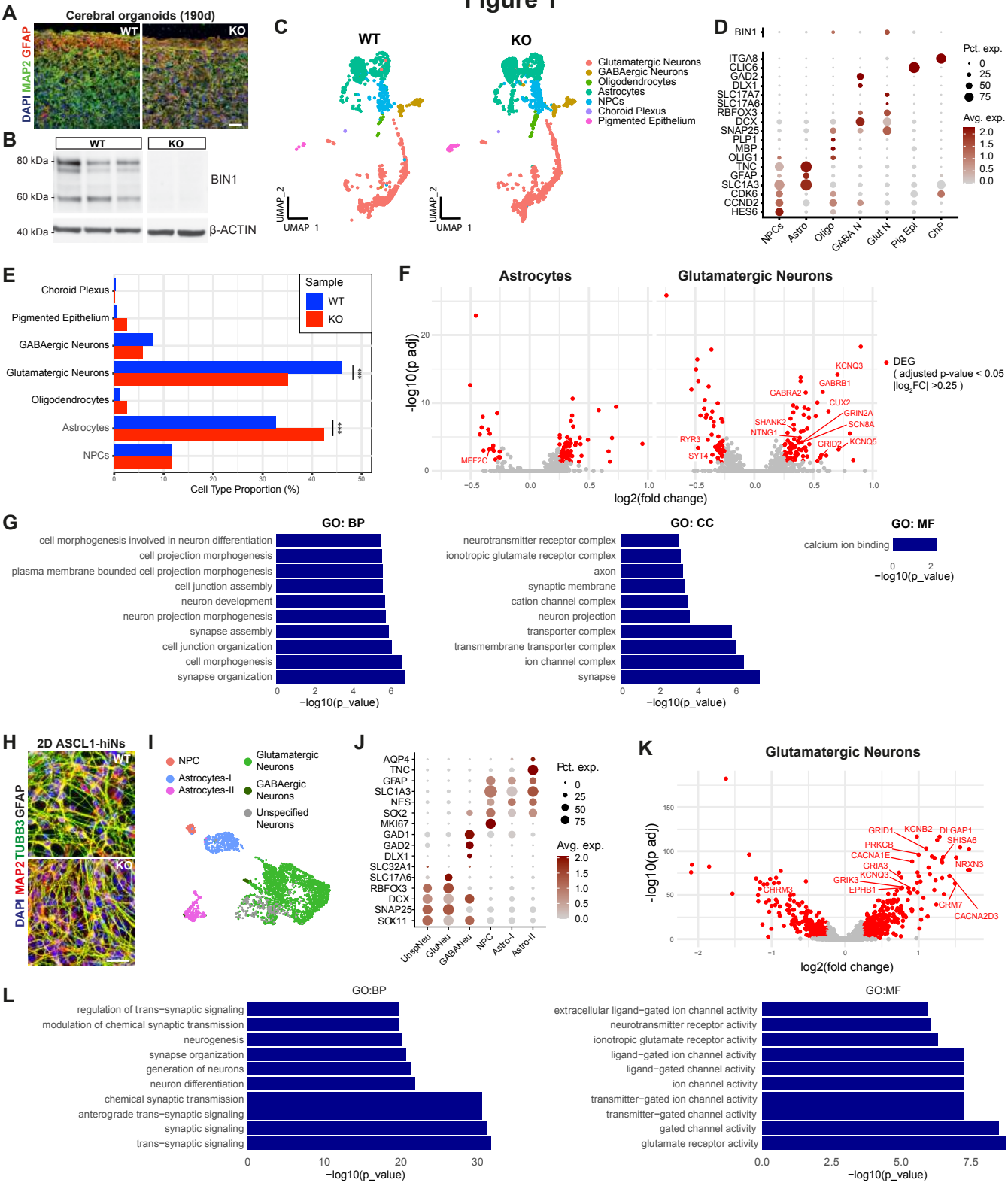
A
Cerebral organoids (190d)
WT
KO
DAPI MAP2 GFAP
B
WT
KO
80 kDa
60 kDa
40 kDa
BIN1
β-ACTIN
C
WT
KO
UMAP_2
UMAP_1
Glutamatergic Neurons
GABAergic Neurons
Oligodendrocytes
Astrocytes
NPCs
Choroid Plexus
Pigmented Epithelium
D
BIN1
ITGA8
CLIC6
GAD2
DLX1
SLC17A7
SLC17A6
RBFOX3
DCX
SNAP25
PLP1
MBP
OLIG1
TNC
GFAP
SLC1A3
CDK6
CCND2
HES6
NPCs
Astro
Oligo
GABA N
Glut N
Pig Epi
ChP
Pct. exp.
0
25
50
75
Avg. exp.
2.0
1.5
1.0
0.5
0.0
E
Sample
WT
KO
Choroid Plexus
Pigmented Epithelium
GABAergic Neurons
Glutamatergic Neurons
Oligodendrocytes
Astrocytes
NPCs
***
***
Cell Type Proportion (%)
F
Astrocytes
Glutamatergic Neurons
-log10(p adj)
log2(fold change)
DEG
(adjusted p-value < 0.05
|log2FC| >0.25)
MEF2C
RYR3
SYT4
KCNQ3
GABRB1
GABRA2
CUX2
GRIN2A
SHANK2
SCN8A
NTNG1
GRID2
KCNQ5
G
GO: BP
cell morphogenesis involved in neuron differentiation
cell projection morphogenesis
plasma membrane bounded cell projection morphogenesis
cell junction assembly
neuron development
neuron projection morphogenesis
synapse assembly
cell junction organization
cell morphogenesis
synapse organization
−log10(p_value)
GO: CC
neurotransmitter receptor complex
ionotropic glutamate receptor complex
axon
synaptic membrane
cation channel complex
neuron projection
transporter complex
transmembrane transporter complex
ion channel complex
synapse
−log10(p_value)
GO: MF
calcium ion binding
−log10(p_value)
H
2D ASCL1-hiNs
WT
KO
DAPI MAP2 TUBB3 GFAP
I
NPC
Astrocytes-I
Astrocytes-II
Glutamatergic Neurons
GABAergic Neurons
Unspecified Neurons
J
AQP4
TNC
GFAP
SLC1A3
NES
SOX2
MKI67
GAD1
GAD2
DLX1
SLC32A1
SLC17A6
RBFOX3
DCX
SNAP25
SOX11
UnspNeu
GluNeu
GABANeu
NPC
Astro-I
Astro-II
Pct. exp.
0
25
50
75
Avg. exp.
2.0
1.5
1.0
0.5
0.0
K
Glutamatergic Neurons
-log10(p adj)
log2(fold change)
GRID1
KCNB2
DLGAP1
SHISA6
PRKCB
CACNA1E
GRIA3
NRXN3
KCNQ3
GRIK3
EPHB1
CHRM3
GRM7
CACNA2D3
L
GO:BP
regulation of trans−synaptic signaling
modulation of chemical synaptic transmission
neurogenesis
synapse organization
generation of neurons
neuron differentiation
chemical synaptic transmission
anterograde trans−synaptic signaling
synaptic signaling
trans−synaptic signaling
−log10(p_value)
GO:MF
extracellular ligand−gated ion channel activity
neurotransmitter receptor activity
ionotropic glutamate receptor activity
ligand−gated ion channel activity
ligand−gated channel activity
ion channel activity
transmitter−gated ion channel activity
transmitter−gated channel activity
gated channel activity
glutamate receptor activity
−log10(p_value)

Figure 6

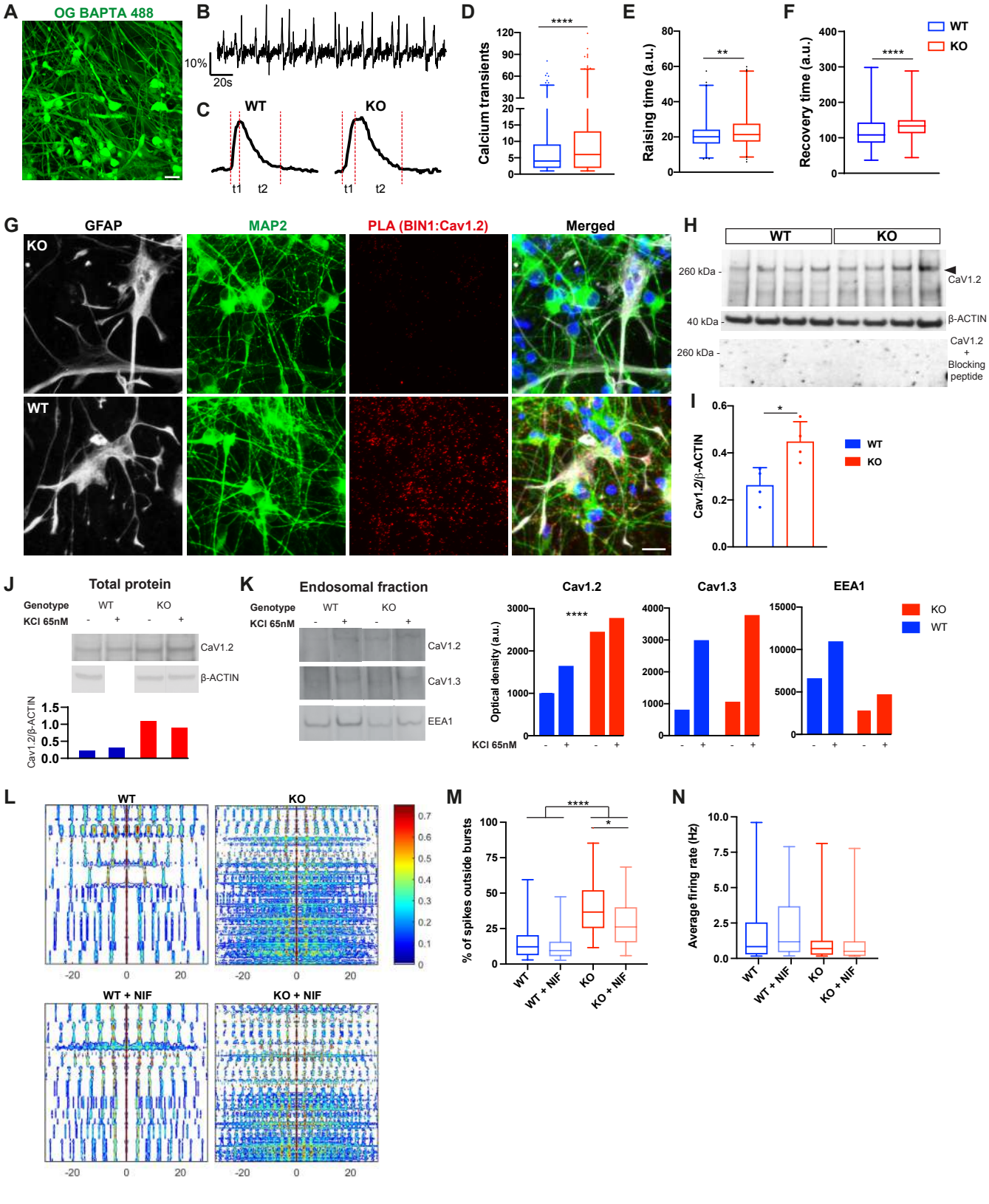
A
OG BAPTA 488
B
10%
20s
C
WT
KO
t1
t2
D
Calcium transients
****
E
Raising time (a.u.)
**
F
Recovery time (a.u.)
****
WT
KO
G
GFAP
MAP2
PLA (BIN1:Cav1.2)
Merged
KO
WT
H
WT
KO
260 kDa
CaV1.2
40 kDa
β-ACTIN
260 kDa
CaV1.2 + Blocking peptide
I
Cav1.2/β-ACTIN
*
WT
KO
J
Total protein
Genotype
WT
KO
KCl 65nM
CaV1.2
β-ACTIN
Cav1.2/β-ACTIN
K
Endosomal fraction
Genotype
WT
KO
KCl 65nM
CaV1.2
CaV1.3
EEA1
Cav1.2
Cav1.3
EEA1
Optical density (a.u.)
****
KCl 65nM
KO
WT
L
WT
KO
WT + NIF
KO + NIF
M
% of spikes outside bursts
****
*
WT
WT + NIF
KO
KO + NIF
N
Average firing rate (Hz)
WT
WT + NIF
KO
KO + NIF